https://doi.org/10.5194/egusphere-2024-873
Preprint. Discussion started: 3 April 2024

Characterizing the scale of regional landslide triggering from storm hydrometeorology

Jonathan Perkins[1], Nina Oakley[2,3], Brian Collins[1], Skye Corbett[1], W. Paul Burgess[2]

[1]U.S. Geological Survey, Geology, Minerals, Energy, and Geophysics Science Center, Moffett Field, CA, 94035, USA
[2]Center for Western Weather and Water Extremes, Scripps Institute of Oceanography, San Diego, CA, 92037, USA
[3]California Geological Survey, Sacramento, CA, 95814, USA

Correspondence to: Jonathan Perkins (jperkins@usgs.gov)

Abstract. Rainfall strongly affects landslide triggering; however, understanding how storm characteristics relate to the severity of landslides at the regional scale has thus far remained unclear, despite the societal benefits that would result from defining this relationship. As mapped landslide inventories typically cover a small region relative to a storm system, here we develop a proxy for landslide-inducing rainfall, A^*, based on extremes of modelled soil water relative to its local climatology. We calibrate A^* using four landslide inventories, comprising over 11,000 individual landslides over four unique storm events, and find that a common threshold can be applied to estimate regional shallow landslide triggering potential across diverse climatic regimes in California (USA). We then use the spatial distribution of A^*, along with topography, to calculate the landslide potential area (*LPA*) for nine landslide-inducing storm events over the past twenty years, and test whether atmospheric metrics describing the strength of landfalling storms, such as integrated water vapor transport, correlate with the magnitude of hazardous landslide-inducing rainfall. We find that although the events with the largest *LPA* do occur during exceptional atmospheric river (AR) storms, the strength of landfalling atmospheric rivers does not scale neatly with landslide potential area, and even exceptionally strong ARs may yield minimal landslide impacts. Other factors, such as antecedent soil moisture driven by storm frequency, and mesoscale precipitation features within storms, are instead more likely to dictate the patterns of landslide-generating rainfall throughout the state.

1 Introduction

Rainfall-induced landslides are a global hazard that result in thousands of fatalities (Petley, 2012; Froude and Petley, 2018) and billions of dollars in economic losses annually (Schuster and Fleming, 1986; Kjekstad and Highland, 2009). During the progression of a hazardous storm, shallow landslides, those occurring primarily within a soil-mantled hillslope, are often triggered by infiltrating rainwater that interacts with the shallow (typically less than 3 m) groundwater system to produce destabilizing pore water pressures (Reid, 1994; Iverson, 2000; Collins and Znidarcic, 2004; Bogaard and Greco, 2016) (Fig. 1). Over the past five decades, a growing recognition of rainfall-induced landslide hazards has led to a range of efforts in developing landslide warning systems that assess when these rainfall thresholds for slope failure might be exceeded using a

https://doi.org/10.5194/egusphere-2024-873
Preprint. Discussion started: 3 April 2024

variety of criteria (Campbell, 1975; Keefer, 1987; Baum and Godt, 2010; Kirschbaum and Stanley, 2018; Guzzetti et al., 2020, and references therein).

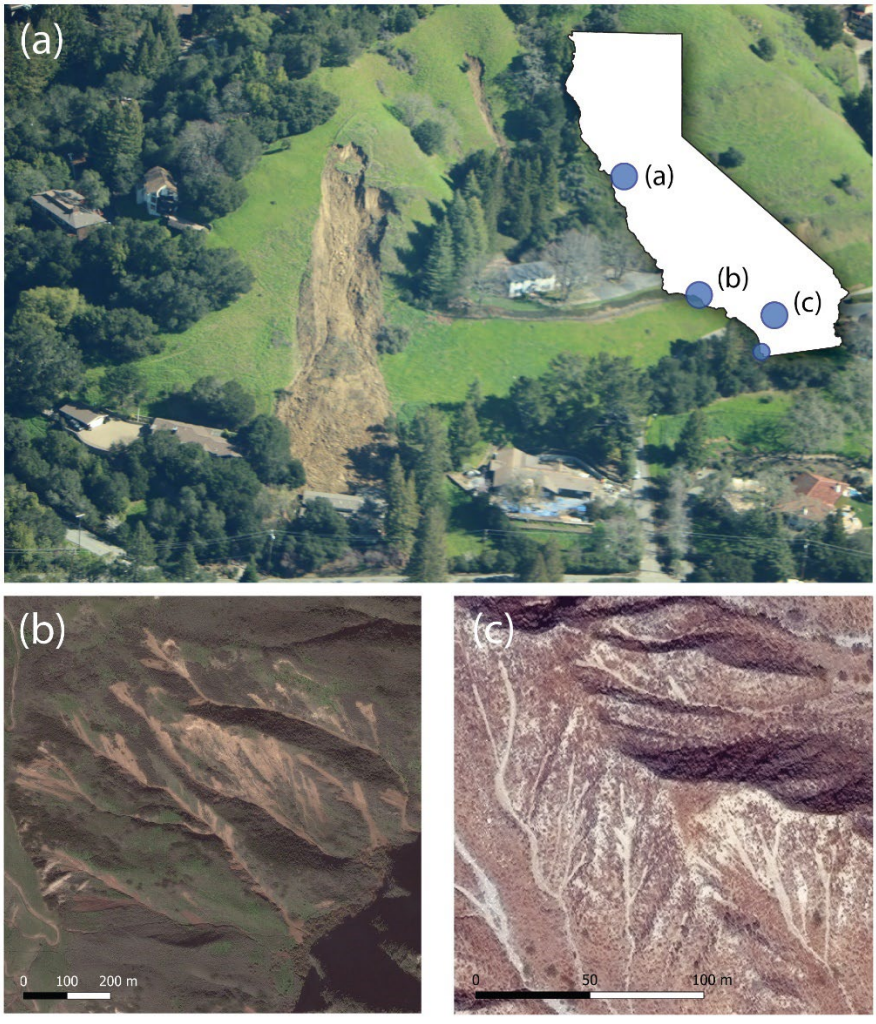

Figure 1. Examples of landslides triggered by recent storms in California. (a) Aerial photograph of a home in California's East Bay region damaged by a landslide initiated during an atmospheric river storm on 06 February 2017. Photo by Brian Collins (Public Domain). (b) Worldview-2 imagery of landslides triggered by heavy rainfall on 10 January 2005, near the town of La Conchita. (c) Worldview-3 imagery of the southernmost San Bernardino Mountains north of Cabazon showing debris flows triggered by the 14 February 2019, atmospheric river storm that caused extensive damage across Riverside County. Inset shows a map of California with annotated circles corresponding to the respective panel. Unlabelled small blue circle corresponds to the location of the landslide inventory associated with a storm in April 2020 that triggered numerous landslides near the town of Encinitas (Fig. 2d).

https://doi.org/10.5194/egusphere-2024-873
Preprint. Discussion started: 3 April 2024

Whereas operational forecasting of landslides using numerical weather prediction remains rare (e.g., Guzzetti et al., 2020; Kong et al., 2020), a growing body of research suggests that distinct meteorological features at both the synoptic scale (~200 to 2000 km, multiple days) and the mesoscale (~2-200 km, minutes to hours) can exert a strong control on landslide occurrence and distribution and could potentially be used for landslide forecasting. For example, atmospheric rivers (ARs) are synoptic features consisting of long filaments of enhanced water vapor in the lower atmosphere and are typically associated with mid-latitude cyclones that transport moisture poleward from the tropics to the mid-latitudes such as the west coast of the United States. They are a primary generator of precipitation in California (USA) and are typically measured and denoted by integrated water vapor transport (IVT) values exceeding 250 kg m^{-1} s^{-1} (Ralph et al. 2019). Combining news reports of landslide events going back over 150 years with an AR catalogue, Cordeira et al. (2019) showed that in California's San Francisco Bay area 70-80% of reported landslide days occur in association with AR conditions. Similarly, Oakley et al. (2018) found that 60-90% of rainfall events exceeding published landslide-triggering thresholds in California over a 22-year period coincided with storms featuring ARs. At a smaller scale, mesoscale processes that operate within synoptic storms and that are shorter-lived phenomena compared to ARs, can provide bursts of higher intensity rainfall that can also trigger abundant landsliding. Collins et al. (2020) found a tight spatial clustering between distributed shallow landslides from a 2018 storm in central California and the stalling of a narrow cold-frontal rainband (NCFR; a band of intense convective rainfall that can occur ahead of a cold front) that followed the passage of an atmospheric river over the region. Here, the timing of landslide triggering coincided with the NCFR rather than the AR, though rainfall associated with the AR likely primed susceptible slopes for later triggering (Collins et al., 2020). Thus, storm characteristics at both the synoptic scale and mesoscale can play an important role in shallow landslide occurrence and distribution, and efforts to forecast landslide occurrence could benefit from assessing the likelihood of these meteorological processes occurring over particular landscapes.

Quantifying both the overall strength of storms and the scale of landslide response across the entire landscape that experienced a storm passage remains an ongoing challenge. One way to characterize distributed storm strength is with the R-CAT scale (Ralph and Dettinger, 2012; Lamjiri et al., 2020), which uses three-day precipitation totals from distributed rain gauges to delineate broad categories of storm strength, from R-CAT 1 to R-CAT 4. This allows intercomparison of extreme rainfall events over the past century when sufficient gauge data exist. On a broader scale, the atmospheric river (AR) scale (Ralph et al., 2019) uses the magnitude and duration of the vertically integrated water vapor transport, IVT, to categorize the relative strength of atmospheric rivers on a scale of AR1 to AR5 at a point. This avoids the dependence of storm impact prediction dependence on site-specific rain gauge data. In the AR Scale, values are suggested to correspond to a balance between beneficial and hazardous conditions, where AR1 is cast as primarily beneficial rainfall and AR5 represents primarily hazardous rainfall, although the authors stress that these are only general guidelines and may often not be the case (Ralph et al., 2019). Although the R-CAT and AR scales allow for intercomparison of storm rainfall or IVT characteristics, they do not specifically represent landslide hazard. For example, if an R-CAT 4 or an AR5 event occurs when soil conditions

https://doi.org/10.5194/egusphere-2024-873
Preprint. Discussion started: 3 April 2024

are dry, they might produce fewer (or no) landslides than if elevated soil moisture conditions were present preceding the storm event. These considerations warrant a more hazard-focused characterization of storms. A primary aim of this study is to develop a simple hydrometeorological metric for conditions consistent with regional shallow landslide occurrence that can be mapped in space and time. We then investigate meteorological characteristics of landslide events used to develop this metric for more in-depth characterization of how landslide occurrence and spatial extent relates to meteorological process strength and spatial extent.

Evaluating the magnitude of landslide hazard potential across the footprint of a given storm event requires some way to estimate landslide triggering. Rainfall intensity-duration thresholds are a common method used to assess the landslide potential for a given storm event (Cannon and Ellen, 1985; Keefer et al., 1987; Larsen and Simon, 1993; Guzetti et al., 2008; Bogaard and Greco, 2018). These relationships are typically calibrated regionally (or at a specific site near a rain gauge) and generally follow a power-law relationship where the triggering rainfall intensity declines exponentially with storm duration. This exponential relationship between rainfall intensity and duration for landslide-triggering implies that higher-intensity storms require less rainfall depth to trigger landslides than lower-intensity storms. This is known to be related to the nonlinear soil moisture storage characteristics that dictate the transmission rate of infiltrating pore water (Green and Ampt, 1911; Richardson, 1922; Richards, 1931; Lu et al., 2011). In landscapes that do not rapidly drain between storm events, antecedent rainfall may lower the amount of rainfall needed to reach critically unstable pore water pressure (Crozier and Eyles, 1980; Crozier, 1999; Glade et al., 2000).

Incorporating antecedent moisture into regional estimates of slope stability has taken several forms. Thomas et al. (2018) considered antecedent soil moisture and rainfall depth thresholds for driving positive pore water pressure in soil columns using physically based infiltration models (i.e., using the Richards equation; Richards, 1931). They found a nonlinear relationship between antecedent soil moisture and the necessary rainfall depth to generate pore water pressures that trigger shallow landslide initiation in California's San Francisco Bay region. The nonlinearity results from the shape of the soil water characteristic curves: as soil saturates from dry to wet conditions, the soil hydraulic conductivity increases by several orders of magnitude (e.g., van Genuchten, 1980), resulting in increasingly fast transmission of pore water from the surface to the water table. The Antecedent Water Index (*AWI*) proposed by Godt et al. (2006) uses only rainfall data in a one-dimensional mass balance model initially derived by Wilson and Wieczorek (1995) that tracks theoretical predictions of soil water throughout a rainy season. This class of reduced complexity soil hydrologic models are commonly referred to as "leaky barrel" or "tank" models, where rainfall immediately enters the model reservoir and drains at a rate proportional to the reservoir height. While *AWI* does not directly incorporate the physical processes of rainfall infiltration into the soil surface (i.e., it does not use the nonlinear soil water characteristic curve relationships upon which the Richards equation is based), the model has nevertheless proven to capture the dynamics of a range of soil hydrologic processes. Where Wilson and Wieczorek (1995) calibrated their model to observed changes in pore water pressure for a landslide early warning system in the San Francisco Bay Area, Godt et al. (2006) calibrated *AWI* to local measurements of soil water content and used an *AWI* threshold as part of a decision tree to forecast landslide events in the Seattle, Washington (USA) region.

https://doi.org/10.5194/egusphere-2024-873
Preprint. Discussion started: 3 April 2024

Similarly, the Japanese Meteorological Agency used a three-tank model calibrated to a specific watershed to develop a soil water index (*SWI*) that has been used to help establish rainfall-induced landslide thresholds across the country (Okada, 2001; Saito and Matsuyama, 2010).

Regional variability also plays a role in setting rainfall thresholds, and several studies have used various forms of normalization of rainfall and/or soil moisture variables to account for this variability (Cannon et al., 1985; Keefer, 1987; Wilson, 1997; Guzetti et al., 2008; Saito and Matsuyama, 2012; Peruccacci et al., 2017). Cannon (1988) normalized rainfall totals by the gauge-specific mean annual precipitation (MAP) to account for regional differences in triggering rainfall. Wilson and Jayko (1997) later updated Cannon's maps using the "rainy day normal" (*RDN* = MAP/number of rainy days) to further account for regional differences in triggering. They noted that that the recurrence interval of storm events is important in the equilibrium of landscapes. Marc et al. (2019) tested the efficacy of the 10-year recurrence, 48-hour rainfall anomaly (R^*_{48}) as a predictor of shallow landslide concentration in Japan and showed that a strong correlation exists between landslide concentration and the magnitude of the rainfall anomaly. For the same storm, Saito and Matsuyama (2012) showed that normalizing the *SWI* by its locally maximum value over the preceding decade also correlated with clustering of landslides.

Wilson and Jakyo (1988), Peruccacci et al. (2017) and Marc et al. (2019) all posited that landscapes must be geomorphically tuned to extreme rainfall, and there are a number of potential reasons why long-term rainfall rates might shape landscapes in ways that result in varying landslide triggering thresholds across climates. For example, soil production and hence soil thickness can change with increasing precipitation (Richardson et al., 2019; Pelletier et al., 2015). Furthermore, root reinforcement of hillslopes is controlled by vegetation density (e.g., Schmidt et al., 2001), which also varies with precipitation (Nemani et al., 2002; Tao et al., 2016). Additionally, theoretical and numerical work shows that local rainfall intensity can alter long-term landscapes by changing factors like drainage density and mean slope (Tucker and Slingerland, 1997), which in turn can lead to nonlinear increases in runoff (Carlston, 1963) that can subsequently drive shallow landslide and debris flow initiation. Thus, there is strong conceptual basis for the normalization of rainfall thresholds with respect to the regional climatology of their respective landscapes.

Combining aspects of both the rainfall anomaly approach of Marc et al. (2019) as well as Saito and Matsuyama (2012), here we calibrate a regional proxy for landslide triggering based on anomalous values of theoretical soil water based on the Antecedent Water Index of Godt et al. (2006) and Wilson and Wieczorek (1995), which we call A^*. To calibrate the methodology, we use landslide inventories from four storms in California that span both arid and temperate regions of the state, a vast and notably geomorphically and climatically diverse region. We show that in the case of our four inventories, a threshold of A^* can be utilized to identify landslide events in both space and time, which bolsters the use of A^* to broadly estimate regionally hazardous rainfall conditions outside the areas of mapped landslides. To estimate the footprint of potentially hazardous (i.e., shallow landslide-inducing) rainfall across the state, we measure the distribution of hillslopes impacted by above-threshold A^* for each storm to define a landslide potential area, LPA. We then apply our methodology to a diverse set of nine impactful landslide-inducing storms across California from 2005-2021. California's landscape

https://doi.org/10.5194/egusphere-2024-873
Preprint. Discussion started: 3 April 2024

encompasses 11 mapped distinct geomorphic provinces distinct in their climatic and topographic characteristics (Jenkins, 1938), and therefore provides an ideal study area in which to evaluate the utility of our hazard index A^* that represents theoretical estimates of anomalous soil water against highly variable climatological conditions. Finally, to examine how the strength of AR conditions relates to the severity of shallow landsliding, we compare the landslide potential area *(LPA*) with the AR Scale (Ralph et al., 2019), and show that while ARs are clearly important drivers of the events in our catalogue, AR climatological frequency rather than individual AR strength, as well as mesoscale features that often define the distribution of brief but intense periods of rainfall, appear to exert a dominant control on shallow landsliding and should therefore be assessed when examining patterns of landslide-inducing rainfall.

2 Methods

2.1 Development of landslide proxy A^* and associated universal threshold

Here we develop a proxy for rainfall-induced shallow landslide potential by establishing a parameter A* that represents extreme values of the Antecedent Water Index (*AWI*) relative to its local climatology:

$$A^* = \frac{AWI}{AWI_{\mathrm{RI}}} \quad (1)$$

where AWI_{RI} is the value of *AWI* at a given recurrence interval (RI). This is similar to the normalized rainfall metric R* proposed by Marc et al. (2019) and also conceptually similar to the normalized soil water index pioneered by Okada (2001) and Saito and Matsuyama (2010); however, here we use the hydrologic tank framework of *AWI* since it does not rely on a specifically calibrated and more complex 3-tank model and has already been effectively utilized in applications of landslide forecasting along the U.S. West Coast (Wilson and Wieczorek, 1995; Godt et al., 2006).

Importantly, A^* does not explicitly assess the susceptibility of individual slopes to rainfall-induced failure as is commonly done for physically based models of shallow slope stability (e.g., Montgomery and Dietrich, 1994; Baum et al., 2008). Rather, the normalization process is purposefully focused on a broader, regional scale. At this coarse spatial scale, we argue that distributions of A^* illustrate overall patterns of hazardous rainfall, which helps provide a framework for intercomparison of storms and the meteorological conditions associated with rainfall-induced landslides.

The *AWI* used in our study was formalized by Godt et al. (2006) to develop a landslide forecast system for Seattle, Washington (USA). The index provides a measure of theoretical soil water using a simple hydrologic tank model developed by Wilson and Wieczorek (1995). The tank model employs a mass balance where rainfall is immediately added to a reservoir with a lower outlet that drains proportionally to the water level in the reservoir. In the model design, reservoir drainage does not occur until sufficient rain has fallen to completely fill soil pores bound by capillarity that restrict water flow. This filling parameter is termed R0 and herein taken to be equal to 0.180 m (Godt et al., 2006) which is approximately the amount of water needed to bring a 1-m-thick loamy soil to field capacity. Once the seasonal rainfall depth exceeds R_0, the flux of additional soil water not bound by capillarity is modelled as follows:

https://doi.org/10.5194/egusphere-2024-873
Preprint. Discussion started: 3 April 2024

$$AWI_t = AWI_{t-1}e^{-k_d\Delta t} + \frac{I_i}{k_d}(1 - e^{-k_d\Delta t}) \quad (2)$$

where I_i is the rainfall rate added to the reservoir [m/hr], k_d is a drainage constant that proportionally modulates the flux out of the system [1/hrs], Δt is the time step [hrs], and the first term in the equation is the value of AWI [m] at the previous timestep (t-1) that has experienced drainage over Δt. Following rainfall, AWI decays back toward the value of R_0. The model assumes that Δt exceeds the timescale required for infiltrating rainwater to integrate fully with the existing pore water in the soil. The model also resets at the beginning of each water year (to R_0), which approximates the impact of processes like evapotranspiration that tend to dry soils from their field capacity back toward their residual moisture content. Whereas constants in eqn. (2) may influence the local magnitude of AWI, for A^* only the relative value is important for a given grid cell, and for the case of the normalized soil water index, the changing rate constants do not significantly impact the normalized parameter (Osanai et al., 2010). Lastly, although this model does not directly consider the physical processes of infiltration into a shallow unconfined aquifer (e.g., Iverson, 2000; Collins and Znidarcic, 2004; Thomas et al., 2018), given that we are modelling changes in seasonal average moisture storage, the model simplifications are reasonable for a depth-averaged estimate of soil moisture, and Wilson and Wieczorek (1995) and Godt et al. (2006) both show that the model can replicate changes in pore water pressure and soil moisture that have been used as part of landslide early warning systems in both northern California and Seattle, Washington, respectively.

Estimating the spatial distribution of AWI_{RI} across our study area required calculating an AWI climatology using a gridded precipitation dataset from which we could estimate local AWI values at varying recurrence intervals. Here we use 4 km grids of six-hourly rainfall from the National Oceanic and Atmospheric Administration (NOAA) California Nevada River Forecast Center (CNRFC) Stage IV Quantitative Precipitation Estimate (QPE) (Seo and Breidenbach, 2002; Nelson et al., 2016; CNRFC, 2023a). These precipitation products are generated by interpolating rain gauge data using the elevation-precipitation relationships established by the PRISM Climate Group (PRISM, 2023). Unlike other NOAA River Forecast Centers, because of poor radar coverage in crucial mountainous areas in California, the CNRFC does not incorporate radar data in their QPE (Nelson et al., 2016). From this archive of gridded precipitation estimates we calculated six-hourly AWI for Water Years 2004-2022 across the state of California. To then calculate AWI_{RI} values for each grid cell, we used a block maxima method (i.e., taking each annual maximum of AWI for each Water Year) to create generalized extreme value distributions from which we calculate local recurrence intervals along each grid cell (e.g., Marc et al., 2019). To be discussed in Section 4.1, for this analysis we selected the 15-year recurrence interval for AWI_{RI}, and the resulting grid was smoothed with a median filter to ensure continuity between pixels.

2.2 Calibration of A^* to four landslide-producing storms in California

We calibrate A^* on a series of four landslide-inducing storms that impacted different regions of California from 2005–2020 (Fig. 2). These events were chosen either because landslide inventories already existed or could be easily mapped from

https://doi.org/10.5194/egusphere-2024-873
Preprint. Discussion started: 3 April 2024

available satellite data. The four calibration events include the January 2005 storm that produced abundant landsliding throughout southern California (Corbett and Perkins, 2024a; Table 1), including the tragic La Conchita landslide that claimed 10 lives during the event (Jibson, 2006); the January 2017 storm that produced thousands of landslides in the East Bay Hills of the San Francisco Bay Area (Corbett et al., 2023; Thomas et al., 2017); the February 2019 storm that produced landslides both in the northern San Francisco Bay Area as well as in southern California's Riverside County (Hatchett et al., 2020; Corbett and Perkins, 2024b); and the April 2020 storm that produced localized landslides and debris flows north of San Diego (CW3E, 2020; California Geological Survey, 2024) (Table 1). These inventories together yield a total of 11,668 individual landslides.

To find a common threshold that is consistent with all four storms and distinguishes landsliding-producing storms from storms that caused no observed landsliding, we first compare the maximum *AWI* for each landslide point (i.e., 11,688 points) during the passage of each storm against its background *AWI* value (as discussed below, we use the 15-year recurrence value). This serves as a simple test whether the triggering *AWI* is a constant threshold across different regions in California, which would plot as a horizontal line, or whether any threshold depends on the background *AWI* itself (sensu Cavagnaro et al., 2023). As the landslide spacing is small relative to the 4 km grid cells of the *AWI* dataset we use the grdtrack function within the PyGMT software package (Uieda et al., 2021) that interpolates a precise value between neighboring grid cells. After identifying an acceptable common *AWI* recurrence interval for normalizing A^* (see Results), we also examined the 19-year time series of A^* across each inventory to illustrate the unique occurrence of these values throughout each of the four calibration storms.

2.3 Calculating the footprint of hazardous rainfall using landslide potential area (*LPA*)

One of the main goals of our study was to develop a methodology for dynamically mapping conditions across the state consistent with distributed shallow landsliding. Our approach was to use A^* as a proxy for distributed shallow landslide occurrence and then calculate the spatial distributions of maximum A^* across a given storm (Table 1). To do this, we identified the time window bracketing the passage of each storm over land (typically on the order of 72 hours; Table 1) and then calculated the maximum of A^* for each pixel in the domain. The landslide potential area (*LPA*) is then calculated simply as the area of hillslopes in our study area (units of km2) with $A^* > 1$. To exclude flat terrain (i.e., not capable of shallow landsliding) and terrain covered in snow (where shallow landslides are unlikely), we created a mask of sloping terrain greater than 5° utilizing a 30 m SRTM-derived digital elevation model (DEM) (Farr et al., 2007), and also excluded grid cells with elevations greater than the typical winter snowline in the state (1024 m; see Hatchett et al., 2017). Whereas the 5° mask is a low threshold for shallow landslide producing hillslopes, we assume a conservative basis given the relatively large DEM grid size compared to typical shallow landslides. This yields a grid of shallow-landslide-prone terrain throughout the study area. To calculate *LPA* [km^2] we then interpolated the grid of A^* maxima to the masked hillslope raster and calculated the area of hillslope cells with an A^* maximum equal to or greater than our defined threshold. While here we do not propose

https://doi.org/10.5194/egusphere-2024-873
Preprint. Discussion started: 3 April 2024

that *LPA* specifically quantifies all areas impacted by landslides, instead we propose this approach offers a reasonable proxy of conditions consistent with observed shallow landsliding that can be used to coordinate potential landslide response.

2.4 Evaluating A^* and *LPA* for a catalogue of recent landslide-triggering storms

We tested our analytical framework for regional shallow landslide triggering on a catalogue of nine landslide-inducing storm events in California since 2005, including the four calibration events described in Section 2.2 (Table 1). Whereas there are notable and well-documented landslide-inducing storms that occurred prior to 2005 in California, the gridded rainfall product we use in our analyses was not available prior to 2005 (Section 2.2.1). Thus, we were limited to evaluating only more recent storms. These storms were selected because they were either exceptionally large storms with a few well-documented landslide occurrences (e.g., October 2021), had mapped landslides with slightly less constrained timing (e.g., February 2005), or were storms with known reports of extensive landsliding but no available inventories (e.g., December 2005).

For each storm in our catalogue, we also examined the synoptic and mesoscale conditions using a variety of meteorological data. This included analysis of several meteorological variables such as geopotential height at various levels, integrated water vapor (IWV) and integrated water vapor transport (IVT), and upper-level winds from the ERA5 reanalysis dataset (Hersbach et al, 2020). We used NEXRAD weather radar data archived at the California-Nevada River Forecast Office (CNRFC, 2023b) and at the National Centers for Environmental Information (NCEI, 2023) to evaluate spatial patterns of rainfall in storms and to identify areas of short-duration, high-intensity rainfall associated with mesoscale features such as narrow cold frontal rainbands or thunderstorms, which are represented by high reflectivity values.

We calculated the AR scale value for each storm using the methodology of Ralph et al. (2019) at all ERA5 grid cells along the California coast for a time window spanning four days preceding the landslide event of interest; the AR scale requires a minimum 72-hour window for calculation. We use the maximum AR scale at landfall in the State as representative of the AR scale of the event. This is common practice in reporting the magnitude of AR events affecting a broad region of interest (e.g., Center for Western Weather and Water Extremes, 2023a), but may differ from the AR scale value calculated at any individual landslide location. Most events affected multiple parts of the State, or the maximum AR scale at landfall corresponded to the location of one or more of the observed landslides. The exception is the April 2020 San Diego County event. In this event, weak AR conditions were present in far northern California during the event window, but were irrelevant to the event itself, with no AR conditions present south of the San Francisco Bay. Thus, it was most appropriate to represent this event as 0, no AR. For the February 2005 Chino Hills event, AR1 conditions were present at a few grid points north of Point Conception, a far distance from the event but still in the broader Southern California region. While this event registered as having AR conditions on the AR scale, this event did not feature synoptic features consistent with an AR. Thus, we rank it as AR1, but do not consider it as an AR in the synoptic features column.

https://doi.org/10.5194/egusphere-2024-873
Preprint. Discussion started: 3 April 2024

Event name and primary impacted regions in CA	Start Date (MM/DD/YYYY)	End Date (MM/DD/YYYY)	Synoptic Features	Mesoscale Features	AR Scale	*LPA* (km^2)
January 2005. Transverse Ranges	01/07/2005	01/11/2005	AR, Closed low	Embedded convection	3	11,950
February 2005. Southern CA, Chino Hills	02/18/2005	02/21/2005	Cutoff low	Embedded convection	1	6,160
December 2005. Northern CA, Coast Ranges, Klamath, Sierra Nevada	12/26/2005	01/03/2006	AR	Ring-like band of moderate rainfall	4	38,600
January 2017. Northern CA	01/08/2017	01/10/2017	AR	Convective bands in Sierra Nevada, San Francisco bay Area	5	25,750
February 2017. Northern CA, San Francisco Bay Area	02/04/2017	02/08/2017	AR	-	5	5,920
March 2018. Central CA coast; western Sierra Nevada foothills	03/21/2018	03/23/2018	AR	Narrow cold frontal rainband	4	1,550
February 2019. Statewide	02/13/2019	02/16/2019	AR	Convective bands in Sierra Nevada, embedded convection in Southern CA	4	5,510
April 2020. San Diego County	04/07/2020	04/11/2020	Cutoff low	Isolated thunderstorms	0	1,620
October 2021. Northern CA San Francisco Bay Area, Sierra Nevada	10/22/2021	10/25/2021	AR	-	5	60

Table 1. Event catalogue of storms used in the analysis. The Synoptic Features column indicates whether the event featured a closed or cutoff low-pressure system, or an atmospheric river (AR), two synoptic-scale features commonly associated with impactful rainfall events in California (CA). The Mesoscale Features column indicates whether a mesoscale feature producing high-intensity rainfall (i.e., reflectivity >45 dBZ) was observed in radar imagery in the area where landslides were observed at the approximate time of landslide occurrence. "Embedded convection" refers to localized areas of high-intensity rainfall embedded within the broader storm system. Dashes indicate no observed features. Also indicated for each event are the measured Atmospheric River (AR) scale using the methodology of Ralph et al. (2019), and the calculated Landslide Potential Area (*LPA*).

https://doi.org/10.5194/egusphere-2024-873
Preprint. Discussion started: 3 April 2024

3 Data: Meteorological characteristics of storms

The nine storms in our catalogue (Table 1) show a range of meteorological characteristics that caused rainfall-induced landslides. The January 2005 and February 2005 storms both impacted southern California; the January 2005 storm caused landslides along the coastal hillslopes and inland canyons of Ventura County (Jibson, 2006; Stock and Bellugi, 2011; Fig. 1) and the February 2005 storm produced hundreds of landslides in the Chino Hills region east of the city of Los Angeles (Prancevic et al., 2019). Both storms featured atmospheric rivers, with AR scale values of AR1 and AR3, respectively. They also exhibited embedded convection at the mesoscale, which can produce short bursts of high-intensity rainfall. Both events were also associated with cutoff- or closed- low pressure systems. Cutoff lows are mid-to-upper-level low pressure systems that are removed from the mean westerly flow and can result in persistent precipitation in a focused area (Oakley and Redmond, 2014; Barbero et al. 2019) thereby potentially affecting the resultant spatial distribution of landsliding. Localized zones of high-intensity precipitation during or in the vicinity of ARs figured prominently in several storms in our catalogue. For example, the December 2005 storm in northern California featured an extreme atmospheric river (AR4) and produced historic flooding and extensive landsliding across the region (Stock and Bellugi, 2011) including in the San Francisco Bay area, in the Klamath River region and in the Sierra Nevada.

The January 2017 and February 2017 events were part of a series of AR storms during the historically wet season of 2016-2017 in the San Francisco Bay area that produced over 9,000 landslides within the East Bay hills region alone (Corbett and Collins, 2023; Fig. 1). In the January 2017 storm in particular, convective bands of high-intensity precipitation were observed in both the Bay Area and the Sierra Nevada foothills. In the March 2018 event, a stalling narrow cold-frontal rainband occurring immediately after the passage of AR conditions (AR4) produced abundant landslides over a section of the Tuolumne River canyon, west of Yosemite National Park (Collins et al., 2020).

The February 2019 AR storm showed evidence of convective bands in the Sierra Nevada (for reference, approximately 150 km east of the photo in Fig. 1a) and embedded convection in southern California, where historic flooding was observed in Riverside County (Hatchett et al., 2020) and hundreds of landslides occurred (Fig. 2c). The April 2020 storm was a cutoff-low pressure system. As the cutoff low passed over the San Diego region, isolated thunderstorms developed, producing high-intensity rainfall and triggering numerous landslides around the town of Encinitas (CGS, 2023; CW3E, 2020). This storm did not reach classification on the AR Scale.

Finally, the October 2021 storms consisted of an AR5 event on 24 October 2021 that that pummeled the U.S. West Coast and was the strongest AR to make landfall in northern California in the past 40 years during the month of October (CW3E, 2021). This storm led to flooding throughout northern California, in addition to landslides in the northern California Coast Ranges and the northern Sierra Nevada.

https://doi.org/10.5194/egusphere-2024-873
Preprint. Discussion started: 3 April 2024

4 Results

4.1 Calibration of A^* and development of regional threshold for shallow landslide-triggering conditions

The triggering *AWI* for landslides from each of the four calibration inventories in our catalogue (January 2005, January 2017, February 2019, and April 2020 storms; Table 1, Fig. 2a-d) varies with the background value of *AWI* for each location (Fig. 2e). Furthermore, the 15-year recurrence value of *AWI* (AWI_{15}) appears to serve as a common threshold (i.e., the 1:1 line) that nearly all mapped landslides exceed across the four events. Whereas the January 2017, February 2019, and April 2020 landslide *AWI* points are closer to this threshold, the January 2005 event plots farther above the 1:1 line. While this appears to suggest that hillslopes with a higher AWI_{15} may have a comparatively higher triggering threshold, evaluation of more landslide events across a broader climatic gradient is required to test this idea sufficiently. We thus take AWI_{15} as the universal normalization parameter in the calculation of A^* for this analysis.

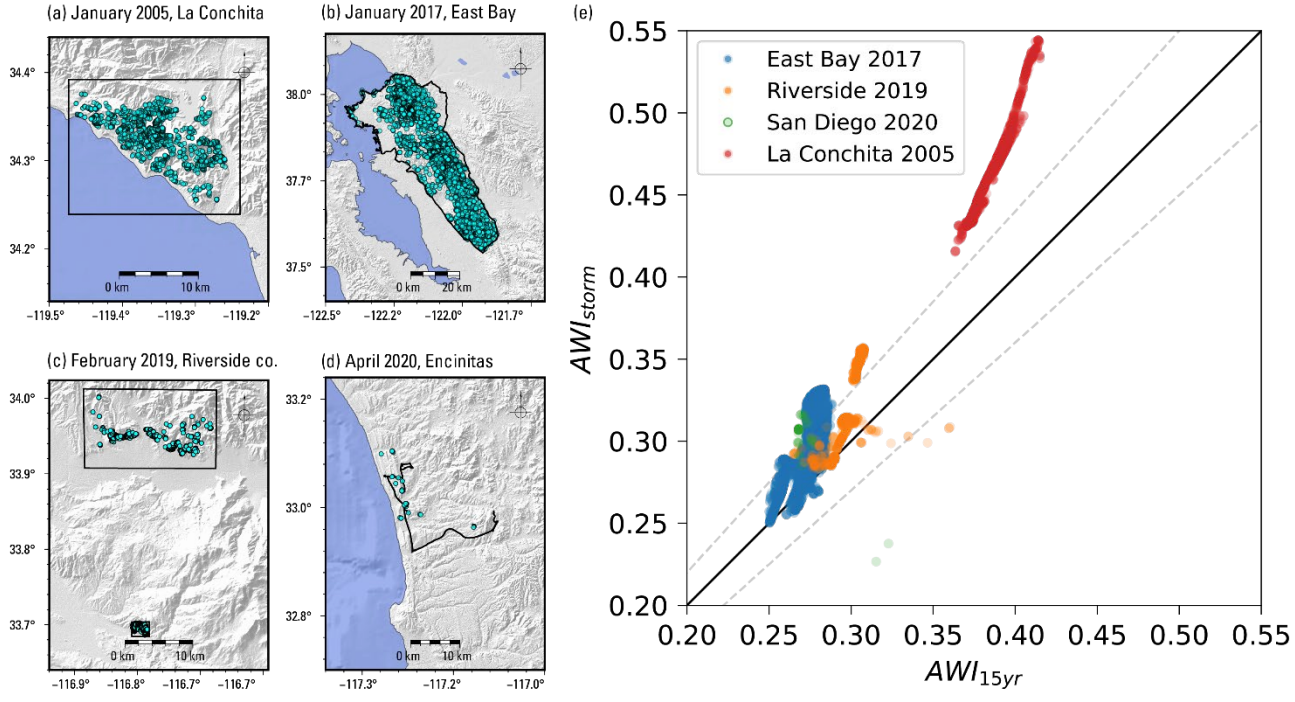

Figure 2. Landslide inventories (a-d) used to estimate a reasonable antecedent water index (*AWI*) recurrence threshold above which most landslides occurred. Panel (e) shows a plot of peak *AWI* modelled during the storm windows interpolated to each landslide point (x-axis) against the 15-year recurrence *AWI* at each point (y-axis). A regionally consistent threshold would plot as a horizontal line, and here most landslides plot above their 15-year recurrence value (the 1:1 line). Dashed lines are the 0.9:1 and 1.1:1 lines. Shaded relief for (a)-(d) derived from NASA SRTM 30 m DEM (NASA, 2013).

https://doi.org/10.5194/egusphere-2024-873
Preprint. Discussion started: 3 April 2024

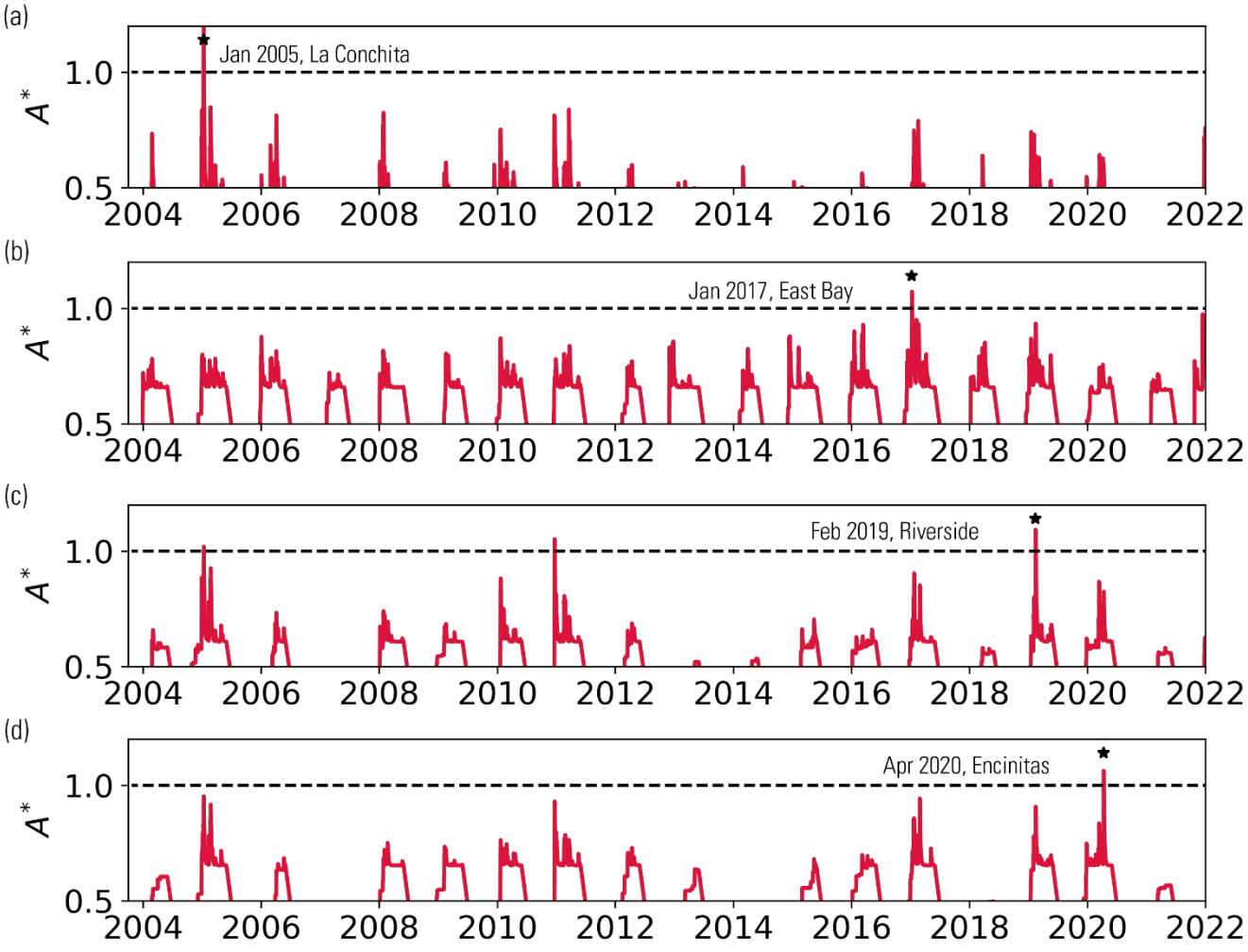

Figure 3. Time series of median A^* within a box surrounding each landslide inventory shown in Fig. 2. Dashed black line corresponds to a threshold value of 1, equivalent to the 15-year recurrence value of modelled antecedent water index (*AWI*) (eqn. 2) at each site. Approximate landslide timing (black star) corresponds to the maximum value of A* across each respective time series. For the case of (b), where landslide observations have been commonplace, no similar instance of extensive landsliding (e.g., Coe and Codt, 2001) has occurred during the modelled interval indicating no false positives. For the case of (c), the above-threshold peak from December 2010 corresponds to a massive regional storm event that produced numerous landslides and flooding in the region, and the 2005 peak corresponds to the same landslide-inducing storm described in (a), which also produced landslides in Riverside County (see discussion in section 4.1).

Because our definition of A^* utilizes a high storm recurrence interval (i.e., 15 years) A^* values above 1 are, by definition, rare. Yet we nevertheless find value in looking at the 20-year time series of A^* across each of our landslide

https://doi.org/10.5194/egusphere-2024-873
Preprint. Discussion started: 3 April 2024

calibration sites for which we have consistent rainfall data. For each of the four calibration events, we find that the landslide-inducing storm exhibited the largest peak in A^* across their respective 20-year histories (Fig. 3). At a minimum, this implies setting an A^* threshold of 1 produces no false positives for each site, with the possible exception of the February 2019 Riverside area (Fig. 3c). Here there are two additional above-threshold peaks in the ~19-year climatology. The early peak coincides with the January 2005 event, and while we do not have landslide mapping from this event in this region, landslides were indeed reported in surrounding Riverside County from this event (e.g., Los Angeles Times, 2005). Similarly, the second peak in A^* occurred in December 2010 and triggered landslides and debris flows across southern California, including in Riverside County, leading to a request for $110 million in federal disaster relief for storm damage (FEMA, 2011). Thus, while we cannot corroborate these two events as producing landslides within the specific boxes due to a lack of detailed landslide inventory information, at the local scale they can be classified as true positives.

When considering false negatives (i.e., distributed shallow landslides for average A^* values less than 1), assessing their outcome becomes more difficult because we do not have detailed histories of landsliding (or absence thereof) at all four sites. However, for the East Bay hills in the San Francisco Bay Area, (Fig. 2d, 3d), we do know that the regional distributed landsliding produced by the January 2017 and February 2017 storms (combined number of landslides > 9000) has not been observed since the winter of 1997-1998 (Coe and Godt, 2001; Corbett and Collins, 2023). Because these storms occurred so closely in time, it is not possible to determine which of the January versus February 2017 storms produced the majority of landslides (Fig. 3l), although both are known to have caused landslides. Notably, both events produced A* values exceeding 1 within the map area (Fig. 4e,h). Overall, we see that mapped landslides from each of these four calibration storms coincide with peaks in A^* in both space and time, and that a common threshold value of A^*=1 based on a comparison to the 15-year climatology can be applied to discriminate the events from storms that occurred in these locations and that did not produce widespread landsliding.

4.2 A^*, Landslide Potential Area, and the impact of atmospheric river strength

All nine storms in our catalogue show at least some patches of above-threshold A^*; however, the magnitude and spatial distribution of A^* is highly variable (Fig. 4). The inter-quartile ranges of A^* for above-threshold hillslopes mostly occur between 1.0 and 1.1, and do not markedly change with the area of impacted hillslopes (Fig. 5). Both the January 2005 and February 2005 storms show larger inter-quartile ranges of A^* with higher absolute values, and interestingly, both storms occurred within two months of each other in the winter of 2005 and impacted the same regions within southern California (Fig. 4d, g). Both storms had embedded convection and favorable orographic conditions (Table 1), which can lead to locally high rainfall totals (Section 4.1). *LPA* values, which represent the total area of hillslopes experiencing above-threshold A^* for each storm, vary by nearly an order of magnitude and range from approximately 60 km2 in the case of the October 2021 event to just over ~38,000 km^2 in the case of the December 2005 storm that led to severe flooding and landslides across northern California (Fig. 4).

https://doi.org/10.5194/egusphere-2024-873
Preprint. Discussion started: 3 April 2024

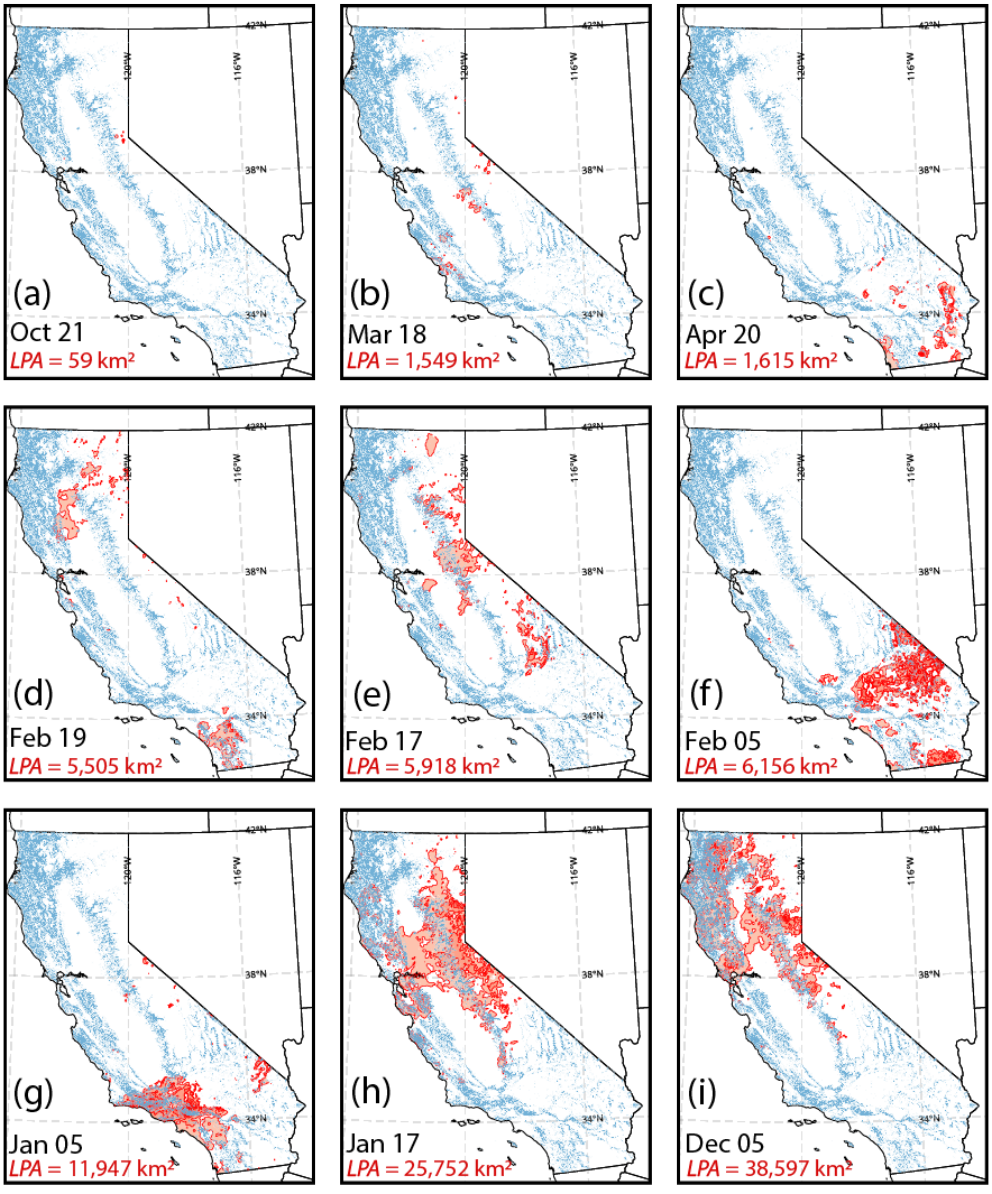

Figure 4. Distributions of A^* and resulting landslide potential area (*LPA*) for the nine landslide-inducing storms in our catalogue (Table 1). Panel numbers (a) – (i) are ranked in order of increasing *LPA*: (a) October 2021, northern California (CA); (b) March 2018, Central Coast and Sierra Nevada; (c) April 2020, Encinitas, (d) February 2019, Riverside County; (e) February 2017, northern CA; (f) February 2005, Chino Hills and eastern CA; (g) January 2005, La Conchita and southern CA; (h) Jan 2017, northern CA; (i) December 2005, northern CA. Red contours show the full spatial distribution of above-threshold A^*, and blue

https://doi.org/10.5194/egusphere-2024-873
Preprint. Discussion started: 3 April 2024

pixels show the hillslopes where *LPA* is calculated. In other words, the *LPA* for each storm is proportional to the total number of blue pixels within the red contours. Topographic data derived from NASA SRTM 30 m DEM (NASA, 2013).

Given that most storms in our catalogue feature ARs, it is logical to investigate how the magnitude of shallow landsliding, as represented by *LPA*, compares to the magnitude of the associated AR conditions (i.e., via the Ralph et al., 2019 scale). Our results show that there is considerable variability between these parameters (Fig. 5). For example, the three storms reaching AR5 (January 2017, February 2017, and October 2021) span the smallest *LPA* to the second largest (Table 1), indicating limited predictability of landslide hazard from measures of IVT alone. One reason for this variability is precisely related to our basing A^* on a model that accounts for antecedent soil moisture conditions. The AR scale does not incorporate any information on antecedent precipitation or soil moisture conditions that may precondition hillslopes and potentially affect subsequent landslide triggering.

Notably, when event *LPA* is plotted against the month in which the storm occurred, a more systematic relationship becomes apparent (Fig. 5b). Within our event catalogue, the largest landslide responses occur in late December and January,

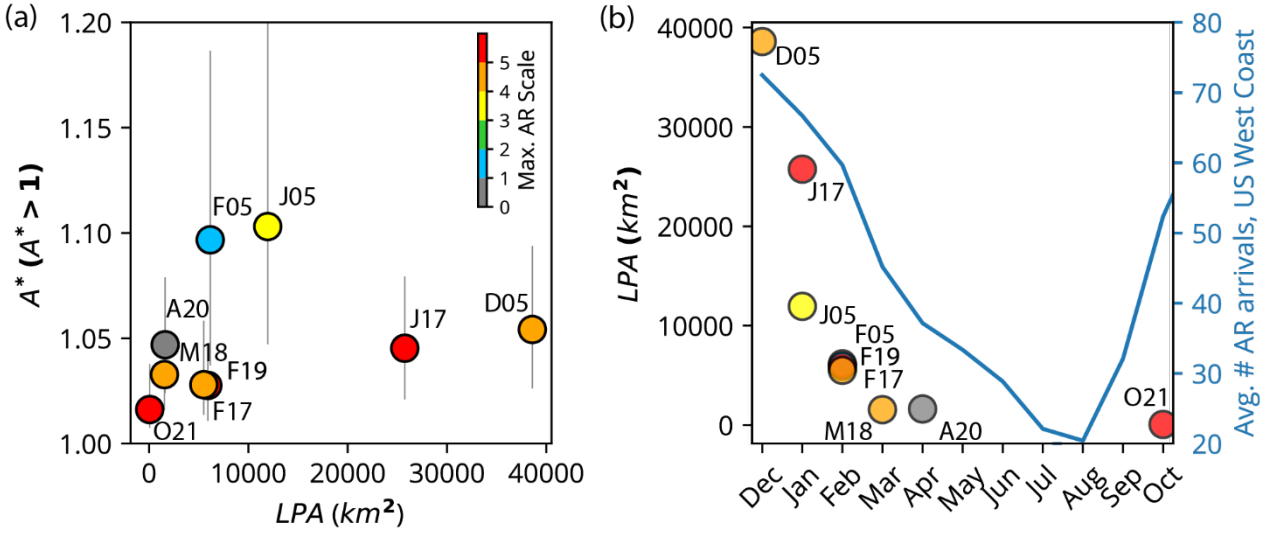

Figure 5. Plots showing the relationship between A^*, landslide potential area (*LPA*), and the Ralph et al. (2019) atmospheric river (AR) scale. Panel (a) shows how the population of above-threshold values of *A (threshold=1) varies with *LPA* and the AR scale (color). Dots show the median value of above-threshold A^*, and vertical lines show the interquartile range. While most events have median values somewhere close to 1, both the January 2005 and February 2005 events have higher median values close to 1.1 and much larger interquartile ranges. This likely reflects the strong orographic and convective nature of these two storms in southern California (see discussion). High AR-scale events exhibit both the highest and lowest values of *LPA* in our catalogue. Panel (b) shows *LPA* variation (left axis) with the time of year. Events in December and January have the highest *LPA*, with decreasing**

https://doi.org/10.5194/egusphere-2024-873
Preprint. Discussion started: 3 April 2024

impacted area (i.e., smaller *LPA*) later in the rainy season. Right axis shows the average annual AR arrivals along the U.S. West Coast from reanalysis data (Mundhenk et al., 2016).

and progressively decline throughout the year in an almost exponential fashion. Although the event catalogue is lacking in spring events relative to winter events, the overall apparent trend indicates that seasonal processes are at play that likely modulate the antecedent soil moisture in landslide-prone hillslopes. This supports our use of a soil moisture (i.e., *AWI*) anomaly-based metric for identifying landslide-inducing storms; soil moisture generally decreases in the spring months (March-April-May) as storms become less frequent (Figure 5b) and evapotranspiration increases with longer days and temperatures. Thus, *LPA* tracks well with storm frequency metrics such as the frequency of AR arrivals along the west coast of the United States (Mundhenk et al., 2016) which peaks in December and January with a decline similar to the monthly decline in *LPA* (Fig. 5b). A similar pattern is seen in the seasonal shallow landslide activity of the Pacific Northwest, indicating the role of groundwater conditions in driving the seasonality of regional shallow landslide activity (Luna et al., 2022). Because A^* and *LPA* represent local extremes of soil water, this consistent trend across all events suggests that the observed seasonality in *LPA* persists across the state despite the large differences in annual rainfall (and *AWI*).

5 Discussion and Conclusions

5.1 Effect of low antecedent moisture on large, early-season storm impacts

The October 2021 AR5 storm offers an important example of how low antecedent soil moisture can blunt the impacts of an exceptional storm producing record precipitation in California's highly seasonal climate (Fig. 6). This storm followed a year of drought and came uncharacteristically early for an AR of its magnitude (e.g., Ralph et al., 2019; CW3E, 2021). Because of this, soils were close to their residual moisture content. Despite generating a wide swath of highly anomalous 48-hour rainfall with R^*_{48} values locally exceeding 3 from the San Francisco Bay area to the Sierra Nevada (Fig. 6a,b), no reports of major landsliding occurred outside of a few isolated events. Notably, Marc et al. (2019) report R^*_{48} values exceeding 2 as an approximate threshold for what should lead to high-density distributed landsliding. In our calculation of A^*, the initially dry soil conditions at the storm onset that occurred only a few weeks into the rainfall season (beginning October 1 in California), contributed to a diminished distribution of A^* and therefore little predicted landsliding (Fig. 5c). Thus, in Mediterranean climates where dry soils can mitigate the hazardous effects of anomalously high rainfall, consideration of soil storage is an important factor when using normalized thresholds for regional prediction of shallow landslides in soil-mantled hillslopes (e.g., Fig. 6b).

https://doi.org/10.5194/egusphere-2024-873
Preprint. Discussion started: 3 April 2024

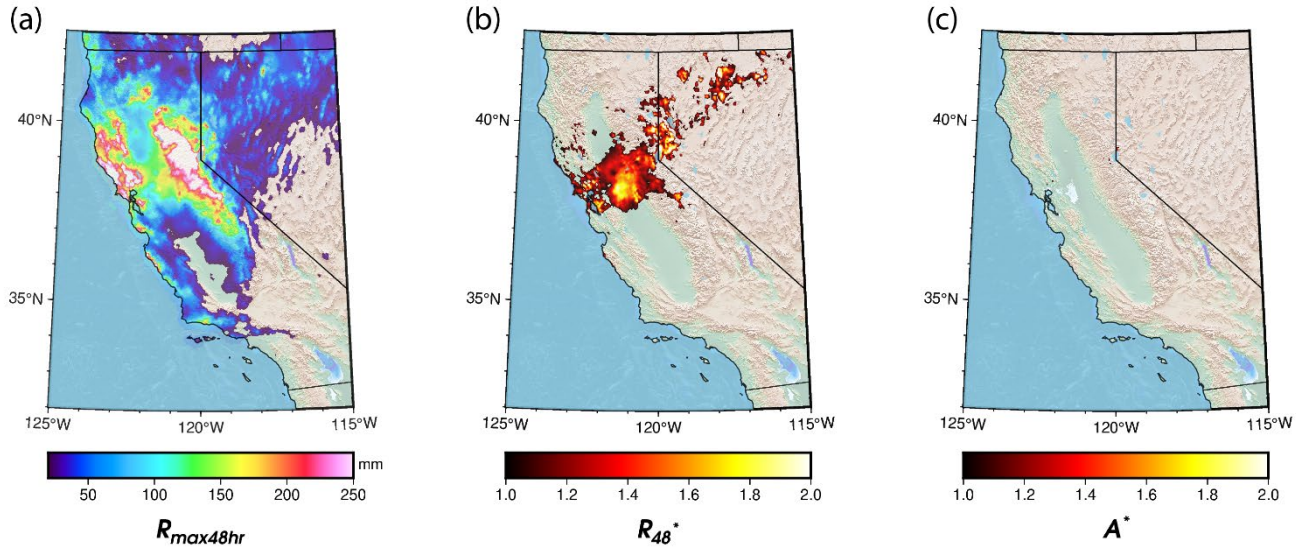

Figure 6. (a) Map showing 48-hour maximum precipitation from the October 25th, 2021 Atmospheric River scale 5 (AR5) that struck northern and central California and produced widespread flooding but few landslides (Table 1). (b) R^*_{48} metric of Marc et al. (2019) showing highly anomalous two-day rainfall totals for the region, calculated by taking the results of panel (a) and dividing by the 10-year recurrence 48-hour rainfall estimates from the NOAA Atlas-14 dataset (Perica et al., 2014). (c) Map of A^* showing that despite anomalously high rainfall, little impact was predicted for distributed shallow landslide occurrence. Shaded relief for all plots from NASA SRTM 30 m DEM (NASA, 2013).

5.2 Dissecting the role of synoptic and mesoscale meteorological processes on landslide hazard

Our study of a wide range of landslide-inducing storms allows evaluation of the role that storm characteristics might have on the distribution of landslides. We found that whereas AR presence is often associated with landslide events (e.g., as in Cordeira et al. 2019), the strength of ARs as measured by the AR Scale did not exert a significant control on the magnitude of landslide-triggering rainfall investigated here. We also find that mesoscale features producing short-duration, high-intensity rainfall may play a more important role in dictating where shallow landslides and associated debris flows occur (Wooten et al., 2008; Coe et al., 2014; Collins et al., 2020). Landslides from the April 2020 storm, one of the events with the smallest LPA values in our catalogue, were triggered by an isolated thunderstorm following a persistent, multi-day period of rainfall associated with a cutoff low-pressure system (CW3E, 2023). The mapped landslides spatially correlate with a roughly 10-km wide area of high (>50 dBZ) radar reflectivity representing the isolated effects of the thunderstorm (Fig. 7a). In a similar example of landslide control by mesoscale processes, extreme rainfall in the March 2018 Central California/Sierra Nevada storm event was influenced by a narrow cold-frontal rainband (NCFR) that stalled over the region (Fig. 7b) following the passage of an AR4 atmospheric river (Collins et al. 2020). Here the pattern of landsliding closely matched the radar reflectivity signature of the NCFR passage across the region. These two cases in particular highlight how

https://doi.org/10.5194/egusphere-2024-873
Preprint. Discussion started: 3 April 2024

synoptic and mesoscale atmospheric features may work together to produced localized landsliding. In each case, the synoptic feature (cutoff-low or atmospheric river) provided long-duration rainfall which sufficiently primed the soils for failure. This was followed by a high-intensity, short-duration burst of rainfall from a mesoscale feature that acted as a landslide trigger (e.g., Collins et al., 2020; Bogaard and Greco, 2018). The resultant footprint of A^* in these two examples thus directly reflects the passage of these synoptic and mesoscale features.

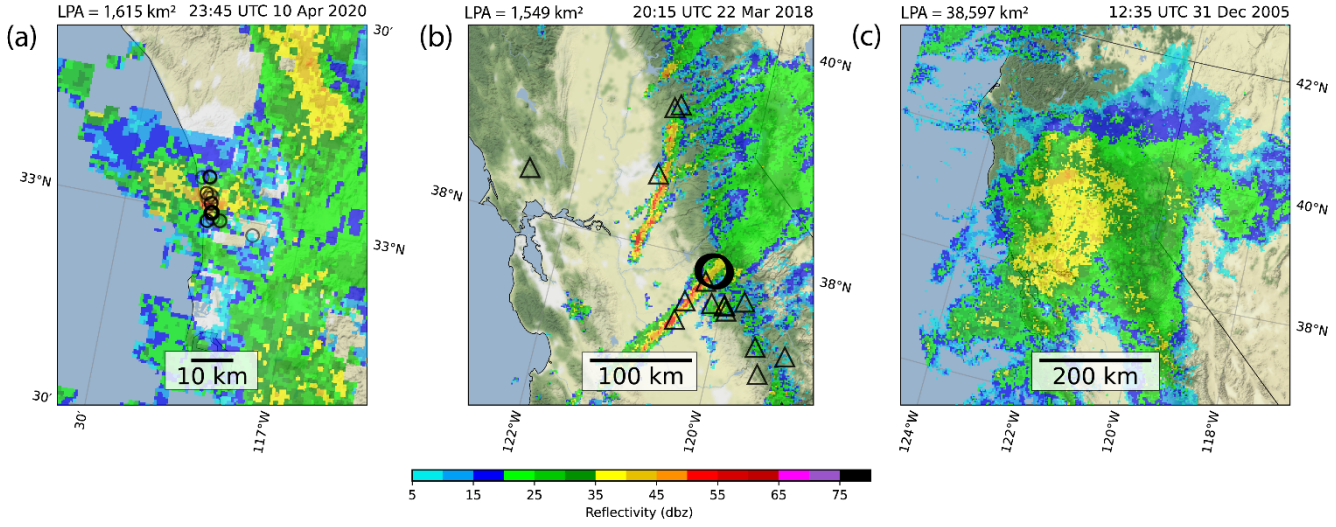

Figure 7. Maps showing examples of a range of spatial scales of precipitation influencing landslide distribution in California. (a) Mesoscale features such as isolated thunderstorms produced very high intensity rainfall and led to localized landslide hotspots in the April 2020 storm in southern California (Table 1; black circles). (b) Narrow cold frontal rainbands (NCFR), on the order of a few km wide and tens of km long, are another mesoscale feature that can produce high-intensity rainfall, leading to regional zones of landsliding as was the case along the Sierra Nevada foothills during the March 2018 event (Table 1). Large circles are mapped landslides from Corbett et al. (2020), and triangles are National Weather Service local storm reports of slope failures during the event (Iowa Environmental Mesonet Cow, 2023). (c) Broad areas of persistent moderate-intensity precipitation may develop under favorable atmospheric conditions, as in the December 2005 storm in northern California (Table 1) and can also lead to widespread distributions of enhanced rainfall that can result in extensive landsliding over a large region and consequently high resultant landslide potential area (*LPA*). Map tiles copyrighted by Stamen Design, 2023, under a Creative Commons Attribution (CC BY4.0) license.

Conversely, the highest-magnitude *LPA* event in the dataset, the December 2005 storm in northern California (*LPA* = 38,600 km^2), was associated with persistent (multi-hour) moderate intensity rainfall over broad areas (~200 km-scale) (Fig. 7c). This may occur due to the persistence of AR conditions over an area or from increased precipitation rates associated with the development of mesoscale frontal waves or secondary cyclones developing near landfalling ARs (e.g., Martin et al. 2019), among other atmospheric processes. The observed rainfall intensities were not as high as the other two events featuring well-defined mesoscale high-intensity rainfall features, but the persistence of moderate-intensity rainfall resulted in

https://doi.org/10.5194/egusphere-2024-873
Preprint. Discussion started: 3 April 2024

excessively anomalous rainfall at the regional scale. Taken together, these results suggest spatial patterns of multi-hour moderate intensity precipitation and short-duration, high-intensity rainfall can both impact a storm's resulting *LPA*. We therefore argue that the mesoscale precipitation characteristics of a storm have the potential to exert a dominant control on its hazard potential and potentially outweigh in some cases the synoptic scale features.

Due to the role of mesoscale processes in driving landslide-inducing rainfall (Wooten et al., 2008; Minder et al., 2009; Coe et al., 2014; Collins et al., 2020), the quality of the quantitative precipitation estimates (QPEs) used in A^* and the resultant *LPA* is important. QPEs that incorporate radar observations may better capture smaller-scale convective features that may not be represented by interpolated rain gauge observations such as the CNRFC 6-hourly QPE (CNRFC, 2023). This is particularly true in landscapes where rain gauges may be heterogeneously distributed. For example, the NCFR passage that drove landsliding in the March 2018 storm was captured well by radar (Fig. 7b) but not particularly well in the rain gage-interpolated precipitation dataset along the Sierra Nevada mountain front where gauge data are relatively sparse (Collins et al., 2020). However, QPE incorporating radar observations may be limited by radar coverage in the complex terrain of the western United States.

5.3 Evaluating A^* performance at the statewide level: an example from the Winter 2023 atmospheric river sequence

Concerns also remain as to the degree of predictive success for A^* across a broader range of events and beyond the relatively small regions (10s to 10,000s km^2) used for model calibration (e.g., Fig. 2). More systematic and complete landslide inventories are therefore needed at the mega-regional scale (i.e., many 100,000 km^2; California is 424,000 km^2 in size) to better evaluate how variations in A^* map with changes in both the presence and absence of landslides and their relative spatial density. Further, if these parameters are utilized in decision-making schemes for evaluating risk and regional warning criteria, more work is required to examine how A^* correlates to landslide triggering across changes in parameters such as topography, lithology and vegetation. For example, Marc et al. (2019) showed that increasing R^* scales with increasing landslide spatial density, and that accounting for lithologic differences further increased correlation. The A^* threshold in this analysis is designed to signify regions of widespread shallow landsliding, but to what extent do increases in A^* correlate with increases in shallow landslide density, and how sensitive a predictor is A^* for more isolated landslide events?

Recently, California experienced an extreme storm sequence of nine back-to-back atmospheric river arrivals from December 2022 to January 2023 (DeFlorio et al., 2024), driving statewide impacts including flooding, landslides and debris flows, and significant wind damage that produced an estimated $5-$7 billion in damages (Moody's RMS, 2023). Throughout the emergency response to the ongoing impacts, the California Geological Survey (CGS) collated and verified reported landslides from State and Federal government agencies (i.e., Brien et al., 2023), social media, California Highway Patrol, news reports, and citizen submissions to include in the CGS Reported Landslides Database (2023). The resulting inventory includes over 700 landslide reports from across the state, mostly nearby road networks where observers were located. Although the inventory does not include a full, detailed accounting of shallow landslides from satellite imagery (e.g., Fig. 2),

https://doi.org/10.5194/egusphere-2024-873
Preprint. Discussion started: 3 April 2024

it covers the entire California study area and thus provides an opportunity to explore how variations in A^* throughout the AR sequence correlate with the location and relative densities of reported landslides.

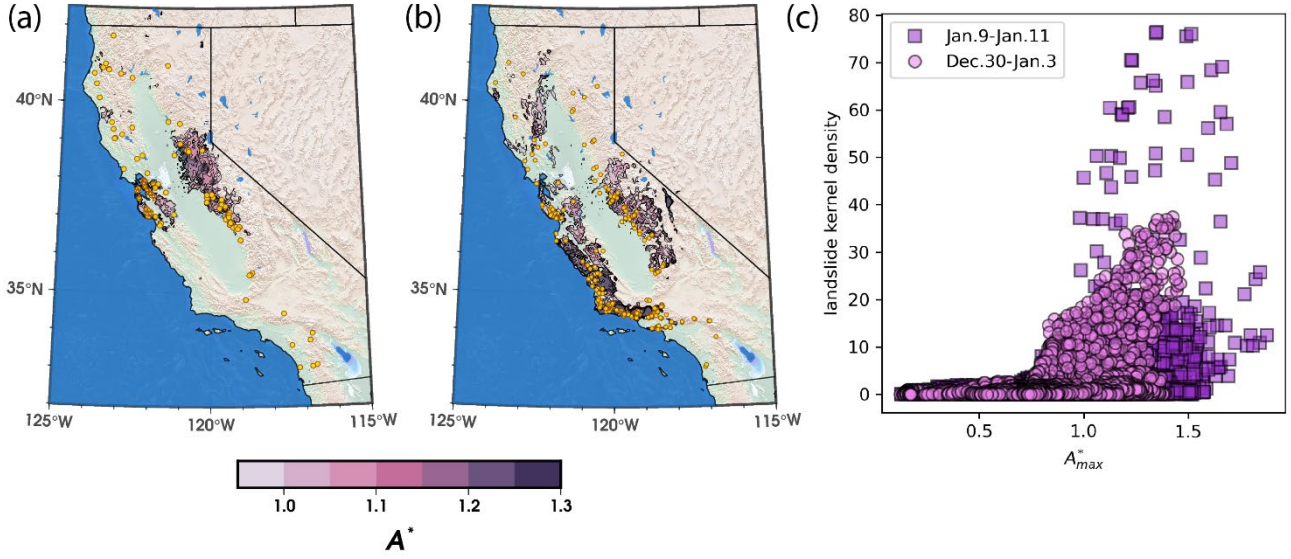

Fig. 8. Maps showing distributions of A^* maxima and reported landslides during two periods of the December 2022 - January 2023 atmospheric river sequence: (a) 30 December – 03 January which strongly impacted the San Francisco Bay area; and (b) 09 January – 11 January, which strongly impacted the central coast and southern California. Yellow symbols are landslides from each time period from the California Geological Survey Reported Landslides. Panel (c) shows a plot relating a grid of landslide point density (y-axis) to A^* maxima for each respective period in the storm sequence. Although a number of isolated slides show low values of A^*, as A^* approaches 1 landslide density begins to rise rapidly. This highlights the efficacy of the method for identifying zones of widespread landsliding rather than locally isolated events. Shaded relief in (a) and (b) from NASA SRTM 30 m DEM (NASA, 2013).

Figure 8 shows snapshots of A^* maxima and reported landslides from the CGS database during two of the most intense storm periods during the 2023 AR sequence: 30 December 2022 – 03 January 2023 (AR3; Fig. 8a), and 09 January – 11 January 2023 (AR3; Fig. 8b). Overall, the footprints of A^* generally cover the zones of high landslide density at the regional scale for both cases. Isolated landslides are not very well-resolved by the method; however, some events in the reported landslide database may be related to roadcut failures and may not reflect purely natural conditions. Additionally, at this level of mapping it is difficult to evaluate false positives (i.e., zones of above-threshold A^* where reported landslides are absent) because of potential reporting biases. For example, landslides may be under-reported in areas of low road or population density, or in instances when certain roads may have already been closed due to storm damage. Future work with a more

https://doi.org/10.5194/egusphere-2024-873
Preprint. Discussion started: 3 April 2024

robust mapping of natural failures across the entire domain (a rare and comprehensive, time-consuming effort) would help quantify prediction uncertainty. Even so, a gross comparison of reported landslide spatial density with increases in A^* (Fig. 8c) shows a marked rise in landslide kernel density as A^* approaches and exceeds a value of 1, our calibrated threshold based on the local 15-year recurrence of *AWI*.

While local site heterogeneity in soil strength and root cohesion are likely to exert a strong second order control on the relationship landslide triggering during extreme rainfall events (e.g., McGuire et al., 2016; Rengers et al., 2016; Perucacci et al., 2017), beyond what is accounted for in the climatic normalization process (eqn. 1; Marc et al. 2019), this analysis suggests that to first order, A^* is an effective metric for delineating zones of widespread landsliding and can hence serve as a useful guide for evaluation of regional hazard potential.

5.4 Towards predicting the effects of rainfall-induced landslide hazards

A primary goal of this analysis was to work towards enhancing situational awareness for rainfall-induced shallow landslide hazard. Global forecast models such as the Global Forecast System (NOAA, 2023) and the European Center For Medium-Range Weather Forecasts (ECMWF, 2024 provide precipitation forecasts out to approximately two weeks and can be used as input to provide forecasts of A^* (and hence *LPA*). Gridded precipitation estimates such as the NOAA Stage IV product (Seo and Breidenbach, 2002; Nelson et al., 2016) could be used to calculate season-to-date A^* in an operational scenario. Although the methods developed herein are only applicable for situational awareness of hazardous rainfall at the scale of the precipitation data used and which are typically coarser than the spatial scale of individual hillslopes, one potential advantage is its simplicity of implementation as only rainfall data are needed as model input for A^*. In future work, a more rigorous investigation of model rate constants and additional controls on the water mass balance such as evapotranspiration could be investigated. This would be particularly important for Mediterranean climates like California, which are projected to see an increasing number of dry days in a warming climate (Polade et al. 2014).

Nevertheless, our analysis shows that A^* provides a good first-order indication of landslide-inducing rainfall for soil-mantled hillslopes across a range of climatic conditions in California. This simple approach could be used with precipitation forecasts and estimates to provide early warning of landslide hazards and support emergency management decisions ahead of potential events. Additionally, the approach presented here can be used to provide insight into the meteorological and climatic processes that control landslide hazard, conduct intercomparisons of past landslide events, or be used for climate model output to assess the potential for increased landslide hazard in future storm events.

Data Availability

Landslide data supporting this manuscript are available as U.S. Geological Survey Data Releases (Corbett and Perkins,2024a and 2024b).

https://doi.org/10.5194/egusphere-2024-873
Preprint. Discussion started: 3 April 2024

Disclaimer

Any use of trade, firm, or product names is for descriptive purposes only and does not imply endorsement by the U.S. Government.

Author Contributions

JP designed and conducted analysis with input from NO, BC, and PB. SC mapped pre-2023 landslides with input from JP, and PB compiled 2023 landslide data and helped with analysis. JP wrote the manuscript with input from all authors.

Competing Interests

The contact author has declared that none of the authors has any competing interests.

Acknowledgements

Samuel Bartlett (CW3E), Dianne Brien (USGS), Karimah Comstock (USGS), and Mikael Witte (NPS) provided helpful discussions throughout the development of this work. Brian Kawzenuk (CW3E) provided AR scale calculations. Reviews by Matthew Thomas (USGS), and Odin Marc (GET), who reviewed a previous version of this paper, helped improve this manuscript.

References

Barbero, R., Abatzoglou, J. T., and Fowler, H. J.: Contribution of large-scale midlatitude disturbances to hourly precipitation extremes in the United States, Clim Dyn, 52, 197–208, https://doi.org/10.1007/s00382-018-4123-5, 2019.

Baum, R. L. and Godt, J. W.: Early warning of rainfall-induced shallow landslides and debris flows in the USA, Landslides, 7, 259–272, https://doi.org/10.1007/S10346-009-0177-0/FIGURES/8, 2010.

Baum, R. L., Savage, W. Z., and Godt, J. W.: TRIGRS — A Fortran Program for Transient Rainfall Infiltration and Grid-Based Regional Slope-Stability Analysis, Version 2.0, U.S. Geological Survey Open-File Report, 75, 2008. Also available at https://pubs.usgs.gov/of/2008/1159/.

Bessette-Kirton, E. K., Cerovski-Darriau, C., Schulz, W. H., Coe, J. A., Kean, J. W., Godt, J. W., Thomas, M. A., and Stephen Hughes, K.: Landslides triggered by Hurricane Maria: Assessment of an extreme event in Puerto Rico, GSA Today, 29, 4–10, https://doi.org/10.1130/GSATG383A.1, 2019.

Bogaard, T. and Greco, R.: Invited perspectives: Hydrological perspectives on precipitation intensity-duration thresholds for landslide initiation: Proposing hydro-meteorological thresholds, Natural Hazards and Earth System Sciences, 18, 31–39, https://doi.org/10.5194/NHESS-18-31-2018, 2018.

Bogaard, T. A. and Greco, R.: Landslide hydrology: from hydrology to pore pressure, Wiley Interdisciplinary Reviews: Water, 3, 439–459, https://doi.org/10.1002/WAT2.1126, 2016.

https://doi.org/10.5194/egusphere-2024-873
Preprint. Discussion started: 3 April 2024

Brien, D. L., Collins, B., Corbett, S., and Perkins, J. P.: San Francisco Bay Area Reconnaissance Landslide Inventory, January 2023, https://doi.org/10.5066/P9NJ3KMG, 2023.

Browning, K. A., Hardman, M. E., Harrold, T. W., and Pardoe, C. W.: The structure of rainbands within a mid-latitude depression, Quarterly Journal of the Royal Meteorological Society, 99, 215–231, https://doi.org/10.1002/QJ.49709942002, 1973.

California Nevada River Forecast Center (CNRFC). http://www.cnrfc.noaa.gov, accessed 6/2/2023.

California Nevada River Forecast Center (CNRFC) Radar Archive, https://www.cnrfc.noaa.gov/radarArchive.php, accessed 6/2/2023.

Campbell, R. H.: Soil slips, debris flows, and rainstorms in the Santa Monica Mountains and vicinity, southern California, Professional Paper, https://doi.org/10.3133/PP851, 1975.

Cannon, S. H.: Regional rainfall-threshold conditions for abundant debris-flow activity, in: Landslides, Floods, and Marine Effects of the Storm of January 3-5, 1982, in the San Francisco Bay Region, California, vol. 1434, 35–42, 1988.

Cannon, S. H. and Ellen, S.: Rainfall Conditions for Abundant Debris Avalanches in the San Francisco Bay Region, California, California Geology, 38, 267–272, 1985.

Carlston, C. W.: Drainage density and streamflow, U.S. Geol. Surv. Prof. Pap. No. 42, 2–C, 8pp, https://doi.org/10.3133/PP422C, 1963.

Cavagnaro, D. B., McCoy, S. W., Thomas, M. A., Kostelnik, J., and Lindsay, D. N.: The spatial distribution of debris flows in relation to observed rainfall anomalies: Insights from the Dolan Fire, California, E3S Web of Conf., 415, 04003, https://doi.org/10.1051/e3sconf/202341504003, 2023.

Center for Western Weather and Water Extremes (CW3E), Storm outlooks and summaries. https://cw3e.ucsd.edu/news/, accessed 6/2/2023.

Center for Western Weather and Water Extremes (CW3E), Characteristics and Impacts of the April 4-11 Cutoff Low Storm in California. https://cw3e.ucsd.edu/characteristics-and-impacts-of-the-april-4-11-2020-cutoff-low-storm-in-california/, accessed 6/2/2023.

Center for Western Weather and Water Extremes (CW3E). CW3E Event Summary: 19-26 October 2021. https://cw3e.ucsd.edu/cw3e-event-summary-19-26-october-2021/, accessed 6/1/2023.

Coe, J. A. and Godt, J. W.: Debris flows triggered by the El Nino rainstorm of February 2-3, 1998, Walpert Ridge and vicinity, Alameda County, California, Miscellaneous Field Studies Map, https://doi.org/10.3133/MF2384, 2001.

Coe, J. A., Kean, J. W., Godt, J. W., Baum, R. L., Jones, E. S., Gochis, D. J., and Anderson, G. S.: New insights into debris-flow hazards from an extraordinary event in the Colorado Front Range, GSA Today, 24, 4–10, https://doi.org/10.1130/GSATG214A.1, 2016.

Collins, B. D. and Znidarcic, D.: Stability Analyses of Rainfall Induced Landslides, Journal of Geotechnical and Geoenvironmental Engineering, 130, 362–372, https://doi.org/10.1061/(asce)1090-0241(2004)130:4(362), 2004.

https://doi.org/10.5194/egusphere-2024-873
Preprint. Discussion started: 3 April 2024

Collins, B. D., Stock, J. D., Weber, L. C., Whitman, K., and Knepprath, N.: Monitoring subsurface hydrologic response for precipitation-induced shallow landsliding in the San Francisco Bay area, California, USA. In E. Eberhardt, C. Froese, K. Turner, & S. Leroueil (Eds.), *Landslides and engineering slopes: protecting society through improved understanding*, (pp. 1249-1255). London, UK: Taylor and Francis Group.

Collins, B. D., Oakley, N. S., Perkins, J. P., East, A. E., Corbett, S. C., and Hatchett, B. J.: Linking Mesoscale Meteorology With Extreme Landscape Response: Effects of Narrow Cold Frontal Rainbands (NCFR), Journal of Geophysical Research: Earth Surface, https://doi.org/10.1029/2020JF005675, 2020.

Corbett, S. C. and Collins, B. D.: Landslides triggered by the 2016–2017 storm season, eastern San Francisco Bay region, California, Scientific Investigations Map, U.S. Geological Survey, https://doi.org/10.3133/sim3503, 2023.

Corbett, S. C., Oakley, N. S., East, A. E., Collins, B. D., Perkins, J. P., and Hatchett, B. J.: Field, geotechnical, and meteorological data of the 22 March 2018 narrow cold frontal rainband (NCFR) and its effects, Tuolumne River canyon, Sierra Nevada Foothills, California, , https://doi.org/10.5066/P9BU8FAQ, 2020.

Cordeira, J. M., Stock, J., Dettinger, M. D., Young, A. M., Kalansky, J. F., and Ralph, F. M.: A 142-year climatology of northern California landslides and atmospheric rivers, Bulletin of the American Meteorological Society, 100, https://doi.org/10.1175/BAMS-D-18-0158.1, 2019.

Corbett, S. C., and Perkins, J.P.: Landslides triggered by the January 11th, 2005 storm in the vicinity of La Conchita, Ventura County, CA, USA. U.S. Geological Survey data release, https://doi.org/10.5066/P9K6E6MW, 2024a.

Corbett, S.C., and Perkins, J.P.: Landslides triggered by the February 2019 atmospheric river storm in the vicinity of Bee Canyon, Riverside County, CA USA. U.S. Geological Survey data release, https://doi.org/10.5066/P92XCRSZ, 2024b.

Crozier, M. J.: Prediction of rainfall-triggered landslides: A test of the antecedent water status model, Earth Surface Processes and Landforms, 24, 825–833, https://doi.org/10.1002/(SICI)1096-9837(199908)24:9<825::AID-ESP14>3.0.CO;2-M, 1999.

DeFlorio, M. J., Sengupta, A., Castellano, C. M., Wang, J., Zhang, Z., Gershunov, A., Guirguis, K., Niño, R. L., Clemesha, R. E. S., Pan, M., Xiao, M., Kawzenuk, B., Gibson, P. B., Scheftic, W., Broxton, P. D., Switanek, M. B., Yuan, J., Dettinger, M. D., Hecht, C. W., Cayan, D. R., Cornuelle, B. D., Miller, A. J., Kalansky, J., Monache, L. D., Ralph, F. M., Waliser, D. E., Robertson, A. W., Zeng, X., DeWitt, D. G., Jones, J., and Anderson, M. L.: From California's Extreme Drought to Major Flooding: Evaluating and Synthesizing Experimental Seasonal and Subseasonal Forecasts of Landfalling Atmospheric Rivers and Extreme Precipitation during Winter 2022/23, Bulletin of the American Meteorological Society, 105, E84–E104, https://doi.org/10.1175/BAMS-D-22-0208.1, 2024.

Dettinger, M. D., Ralph, F. M., Das, T., Neiman, P. J., and Cayan, D. R.: Atmospheric rivers, floods and the water resources of California, Water (Switzerland), 3, https://doi.org/10.3390/w3020445, 2011.

Dettinger, M. D., Martin Ralph, F., Hughes, M., Das, T., Neiman, P., Cox, D., Estes, G., Reynolds, D., Hartman, R., Cayan, D., and Jones, L.: Design and quantification of an extreme winter storm scenario for emergency preparedness and planning exercises in California, Natural Hazards, 60, https://doi.org/10.1007/s11069-011-9894-5, 2012.

https://doi.org/10.5194/egusphere-2024-873
Preprint. Discussion started: 3 April 2024

Engstrom, W. N.: The California Storm of January 1862, Quaternary Research, 46, 141–148, https://doi.org/10.1006/QRES.1996.0054, 1996.

Farr, T. G., Rosen, P. A., Caro, E., Crippen, R., Duren, R., Hensley, S., Kobrick, M., Paller, M., Rodriguez, E., Roth, L., Seal, D., Shaffer, S., Shimada, J., Umland, J., Werner, M., Oskin, M., Burbank, D., and Alsdorf, D. E.: The shuttle radar topography mission, Reviews of Geophysics, 45, https://doi.org/10.1029/2005RG000183, 2007.

Federal Emergency Management Agency.: Disaster Notices in the Federal Register: Disaster 1952. https://www.fema.gov/sites/default/files/2020-09/pda-report_fema-1952-dr_ca.pdf, accessed 22 March, 2024.

Fish, M. A., Wilson, A. M., and Ralph, F. M.: Atmospheric river families: Definition and associated synoptic conditions, Journal of Hydrometeorology, 20, https://doi.org/10.1175/JHM-D-18-0217.1, 2019.

Froude, M. J. and Petley, D. N.: Global fatal landslide occurrence from 2004 to 2016, Natural Hazards and Earth System Sciences, 18, 2161–2181, https://doi.org/10.5194/NHESS-18-2161-2018, 2018.

van Genuchten, M. Th.: A Closed-form Equation for Predicting the Hydraulic Conductivity of Unsaturated Soils, Soil Science Society of America Journal, https://doi.org/10.2136/sssaj1980.03615995004400050002x, 1980.

Gochis, D., Schumacher, R., Friedrich, K., Doesken, N., Kelsch, M., Sun, J., Ikeda, K., Lindsey, D., Wood, A., Dolan, B., Matrosov, S., Newman, A., Mahoney, K., Rutledge, S., Johnson, R., Kucera, P., Kennedy, P., Sempere-Torres, D., Steiner, M., Roberts, R., Wilson, J., Yu, W., Chandrasekar, V., Rasmussen, R., Anderson, A., and Brown, B.: The Great Colorado Flood of September 2013, Bulletin of the American Meteorological Society, 96, 1461–1487, https://doi.org/10.1175/BAMS-D-13-00241.1, 2015.

Godt, J. W., Baum, R. L., and Chleborad, A. F.: Rainfall characteristics for shallow landsliding in Seattle, Washington, USA, Earth Surface Processes and Landforms, 31, 97–110, https://doi.org/10.1002/ESP.1237, 2006.

Green, W. H. and Ampt, G. A.: Studies on Soil Physics. Part I, The Journal of Agricultural Science 4(1):1-24 1911. doi:10.1017/S0021859600001441

Guzzetti, F., Peruccacci, S., Rossi, M., and Stark, C. P.: The rainfall intensity-duration control of shallow landslides and debris flows: An update, Landslides, https://doi.org/10.1007/s10346-007-0112-1, 2008.

European Center for Medium-Range Weather Forecasting (ECMWF). https://www.ecmwf.int/, accessed 22 March, 2024.

Guzzetti, F., Gariano, S. L., Peruccacci, S., Brunetti, M. T., Marchesini, I., Rossi, M., and Melillo, M.: Geographical landslide early warning systems, Earth-Science Reviews, 200, 102973, https://doi.org/10.1016/J.EARSCIREV.2019.102973, 2020.

Hatchett, B. J., Daudert, B., Garner, C. B., Oakley, N. S., Putnam, A. E., and White, A. B.: Winter Snow Level Rise in the Northern Sierra Nevada from 2008 to 2017, Water 2017, Vol. 9, Page 899, 9, 899, https://doi.org/10.3390/W9110899, 2017.

Hatchett, B. J., Cao, Q., Dawson, P. B., Ellis, C. J., Hecht, C. W., Kawzenuk, B., Lancaster, J. T., Osborne, T. C., Wilson, A. M., Anderson, M. L., Dettinger, M. D., Kalansky, J. F., Kaplan, M. L., Lettenmaier, D. P., Oakley, N. S., Ralph, F. M., Reynolds, D. W., White, A. B., Sierks, M., and Sumargo, E.: Observations of an Extreme Atmospheric River Storm With a Diverse Sensor Network, Earth and Space Science, 7, e2020EA001129, https://doi.org/10.1029/2020EA001129, 2020.

Hendy, I. L., Dunn, L., Schimmelmann, A., and Pak, D. K.: Resolving varve and radiocarbon chronology differences during the last 2000 years in the Santa Barbara Basin sedimentary record, California, Quaternary International, 310, 155–168, https://doi.org/10.1016/J.QUAINT.2012.09.006, 2013.

Hobley, D. E. J., Sinclair, H. D., and Mudd, S. M.: Reconstruction of a major storm event from its geomorphic signature: The Ladakh floods, 6 August 2010, Geology, 40, 483–486, https://doi.org/10.1130/G32935.1, 2012.

Huang, X. and Swain, D. L.: Climate change is increasing the risk of a California megaflood, Science Advances, 8, 995, https://doi.org/10.1126/SCIADV.ABQ0995, 2022.

Hwang, T., Band, L. E., Hales, T. C., Miniat, C. F., Vose, J. M., Bolstad, P. V., Miles, B., and Price, K.: Simulating vegetation controls on hurricane-induced shallow landslides with a distributed ecohydrological model, https://doi.org/10.1002/2014JG002824, n.d.

Iowa Environmental Mesonet Cow. https://mesonet.agron.iastate.edu/cow/, accessed on 6/2/2023.

Iowa Environmental Mesonet. https://mesonet.agron.iastate.edu/, accessed on 6/2/2023.

Iverson, R. M.: Landslide triggering by rain infiltration, Water Resources Research, 36, 1897–1910, https://doi.org/10.1029/2000WR900090, 2000.

Jenkins, O. P.: Geomorphic Provinces of California as Outlined on the New State Geologic Map: ABSTRACT, AAPG Bulletin, 22, 1717–1717, https://doi.org/10.1306/3d933068-16b1-11d7-8645000102c1865d, 1938.

Jibson, R. W.: The 2005 La Conchita, California, landslide, Landslides, 3, 73–78, https://doi.org/10.1007/S10346-005-0011-2/FIGURES/10, 2006.

Keefer, D. K., Wilson, R. C., Mark, R. K., Brabb, E. E., Brown, W. M., Ellen, S. D., Harp, E. L., Wieczorek, G. F., Alger, C. S., and Zatkin, R. S.: Real-Time Landslide Warning During Heavy Rainfall, Science, 238, 921–925, https://doi.org/10.1126/SCIENCE.238.4829.921, 1987.

Kirschbaum, D. and Stanley, T.: Satellite-Based Assessment of Rainfall-Triggered Landslide Hazard for Situational Awareness, Earth's Future, 6, https://doi.org/10.1002/2017EF000715, 2018.

Kjekstad, O. and Highland, L.: Economic and social impacts of landslides, Landslides - Disaster Risk Reduction, 573–587, https://doi.org/10.1007/978-3-540-69970-5_30/COVER, 2009.

Kong, V. W. W., Kwan, J. S. H., and Pun, W. K.: Hong Kong's landslip warning system—40 years of progress, Landslides, 17, 1453–1463, https://doi.org/10.1007/s10346-020-01379-6, 2020.

Lamjiri, M. A., Ralph, F. M., and Dettinger, M. D.: Recent Changes in United States Extreme 3-Day Precipitation Using the R-CAT Scale, Journal of Hydrometeorology, 21, 1207–1221, https://doi.org/10.1175/JHM-D-19-0171.1, 2020.

Larsen, M. C. and Simon, A.: A rainfall intensity-duration threshold for landslides in a humid- tropical environment, Puerto Rico, Geografiska Annaler, Series A, 75 A, 13–23, https://doi.org/10.1080/04353676.1993.11880379, 1993.

Los Angeles Times: "Mudslide Buries Houses, Kills 3 in Ventura County". https://www.latimes.com/archives/la-xpm-2005-jan-11-me-rain11-story.html, 2005.

https://doi.org/10.5194/egusphere-2024-873
Preprint. Discussion started: 3 April 2024

Lu, N., Kaya, B. S., and Godt, J. W.: Direction of unsaturated flow in a homogeneous and isotropic hillslope, Water Resources Research, https://doi.org/10.1029/2010WR010003, 2011.

Luna, L. V. and Korup, O.: Seasonal Landslide Activity Lags Annual Precipitation Pattern in the Pacific Northwest, Geophysical Research Letters, 49, e2022GL098506, https://doi.org/10.1029/2022GL098506, 2022.

Malamud, B. D., Turcotte, D. L., Guzzetti, F., and Reichenbach, P.: Landslide inventories and their statistical properties, Earth Surface Processes and Landforms, 29, 687–711, https://doi.org/10.1002/ESP.1064, 2004.

Malamud-Roam, F. P., Lynn Ingram, B., Hughes, M., and Florsheim, J. L.: Holocene paleoclimate records from a large California estuarine system and its watershed region: linking watershed climate and bay conditions, Quaternary Science Reviews, 25, 1570–1598, https://doi.org/10.1016/J.QUASCIREV.2005.11.012, 2006.

Marc, O., Gosset, M., Saito, H., Uchida, T., and Malet, J. P.: Spatial Patterns of Storm-Induced Landslides and Their Relation to Rainfall Anomaly Maps, Geophysical Research Letters, 46, 11167–11177, https://doi.org/10.1029/2019GL083173, 2019.

McGuire, L. A., Rengers, F. K., Kean, J. W., Coe, J. A., Mirus, B. B., Baum, R. L., and Godt, J. W.: Elucidating the role of vegetation in the initiation of rainfall-induced shallow landslides: Insights from an extreme rainfall event in the Colorado Front Range, Geophysical Research Letters, 43, 9084–9092, https://doi.org/10.1002/2016GL070741, 2016.

Minder, J. R., Roe, G. H., and Montgomery, D. R.: Spatial patterns of rainfall and shallow landslide susceptibility, Water Resources Research, 45, https://doi.org/10.1029/2008WR007027, 2009.

Montgomery, D. R. and Dietrich, W. E.: A physically based model for the topographic control on shallow landsliding, Water Resources Research, 30, https://doi.org/10.1029/93WR02979, 1994.

Moody's RMS: Moody's RMS estimates US$5-7 billion in total U.S. economic losses from California Flooding. Moody's RMS, accessed 08 February 2024, www.rms.com/newsroom/press-releases/press-detail/2023-01-25/moodys-rms-estimates-us5-7-billion-in-total-us-economic-losses-from-california-flooding, 2023.

Mundhenk, B. D., Barnes, E. A., and Maloney, E. D.: All-Season Climatology and Variability of Atmospheric River Frequencies over the North Pacific, Journal of Climate, 29, 4885–4903, https://doi.org/10.1175/JCLI-D-15-0655.1, 2016.

NOAA National Centers for Environmental Prediction (NCEP). 2011, updated 2024. NOAA/NCEP Global Forecast System (GFS) Atmospheric Model. https://www.ncei.noaa.gov/products/weather-climate-models/global-forecast, accessed 22 March, 2024.

Nelson, B. R., Prat, O. P., Seo, D. J., and Habib, E.: Assessment and implications of NCEP stage IV quantitative precipitation estimates for product intercomparisons, Weather and Forecasting, 31, https://doi.org/10.1175/WAF-D-14-00112.1, 2016.

NASA Shuttle Radar Topography Mission (SRTM): Shuttle Radar Topography Mission (SRTM) Global, https://doi.org/10.5069/G9445JDF, 2013.

https://doi.org/10.5194/egusphere-2024-873
Preprint. Discussion started: 3 April 2024

Nemani, R., White, M., Thornton, P., Nishida, K., Reddy, S., Jenkins, J., and Running, S.: Recent trends in hydrologic balance have enhanced the terrestrial carbon sink in the United States, Geophysical Research Letters, 29, 106–1, https://doi.org/10.1029/2002GL014867, 2002.

Null, J. and Hulbert, J.: California Washed Away: The Great Flood of 1862, Weatherwise, 60, 26–30, https://doi.org/10.3200/WEWI.60.1.26-30, 2007.

Oakley, N. S., Lancaster, J. T., Hatchett, B. J., Stock, J., Ralph, F. M., Roj, S., and Lukashov, S.: A 22-year climatology of cool season hourly precipitation thresholds conducive to shallow landslides in California, Earth Interactions, 22, https://doi.org/10.1175/EI-D-17-0029.1, 2018a.

Oakley, N. S., Cannon, F., Munroe, R., Lancaster, J. T., Gomberg, D., and Martin Ralph, F.: Brief communication: Meteorological and climatological conditions associated with the 9 January 2018 post-fire debris flows in Montecito and Carpinteria, California, USA, Natural Hazards and Earth System Sciences, https://doi.org/10.5194/nhess-18-3037-2018, 2018b.

Okada, K., Makihara, Y., Shimpo, A., Nagata, K., Kunitsugu, M., and Saito, H.: Soil Water Index, Tenki, 47, 36–41, 2001.

Osanai, N., Shimizu, T., Kuramoto, K., Kojima, S., and Noro, T.: Japanese early-warning for debris flows and slope failures using rainfall indices with Radial Basis Function Network, Landslides, 7, 325–338, https://doi.org/10.1007/s10346-010-0229-5, 2010.

Pelletier, J. D., Broxton, P. D., Hazenberg, P., Zeng, X., Troch, P. A., Niu, G. Y., Williams, Z., Brunke, M. A., and Gochis, D.: A gridded global data set of soil, intact regolith, and sedimentary deposit thicknesses for regional and global land surface modeling, Journal of Advances in Modeling Earth Systems, 8, 41–65, https://doi.org/10.1002/2015MS000526, 2016.

Perica, S., Dietz, S., Heim, S., Hiner, L., Maitaria, K., Martin, D., Pavlovic, S., Roy, I., Trypaluk, C., Unruh, D., Yan, F., Yekta, M., Zhao, T., Bonnin, G., Brewer, D., Chen, L.-C., Parzybok, T., and Yarchoan, J.: Precipitation-Frequency Atlas of the United States. Volume 6 Version 2.3. California, 6, 2014.

Peruccacci, S., Brunetti, M. T., Gariano, S. L., Melillo, M., Rossi, M., and Guzzetti, F.: Rainfall thresholds for possible landslide occurrence in Italy, Geomorphology, 290, 39–57, https://doi.org/10.1016/J.GEOMORPH.2017.03.031, 2017.

Petley, D.: Global patterns of loss of life from landslides, Geology, 40, 927–930, https://doi.org/10.1130/G33217.1, 2012.

Polade, S. D., Pierce, D. W., Cayan, D. R., Gershunov, A., and Dettinger, M. D.: The key role of dry days in changing regional climate and precipitation regimes, Scientific Reports, 4, https://doi.org/10.1038/srep04364, 2014.

Ponziani, F., Pandolfo, C., Stelluti, M., Berni, N., Brocca, L., and Moramarco, T.: Assessment of rainfall thresholds and soil moisture modeling for operational hydrogeological risk prevention in the Umbria region (central Italy), Landslides, 9, 229–237, https://doi.org/10.1007/s10346-011-0287-3, 2012.

Prancevic, J. P., Lamb, M. P., McArdell, B. W., Rickli, C., and Kirchner, J. W.: Decreasing Landslide Erosion on Steeper Slopes in Soil-Mantled Landscapes, Geophysical Research Letters, 47, e2020GL087505, https://doi.org/10.1029/2020GL087505, 2020.

https://doi.org/10.5194/egusphere-2024-873
Preprint. Discussion started: 3 April 2024

PRISM Climate Group, Oregon State University, https://prism.oregonstate.edu, data created 4 Feb 2014, accessed 6 June 2023.

Ralph, F., Rutz, J. J., Cordeira, J. M., Dettinger, M., Anderson, M., Reynolds, D., Schick, L. J., and Smallcomb, C.: A Scale to Characterize the Strength and Impacts of Atmospheric Rivers, Bulletin of the American Meteorological Society, 100, 269–289, https://doi.org/10.1175/BAMS-D-18-0023.1, 2019.

Ralph, F. M. and Dettinger, M. D.: Storms, floods, and the science of atmospheric rivers, Eos, Transactions American Geophysical Union, 92, 265–266, https://doi.org/10.1029/2011EO320001, 2011.

Ralph, F. M. and Dettinger, M. D.: Historical and National Perspectives on Extreme West Coast Precipitation Associated with Atmospheric Rivers during December 2010, Bulletin of the American Meteorological Society, 93, 783–790, https://doi.org/10.1175/BAMS-D-11-00188.1, 2012.

Reid, M. E.: A pore-pressure diffusion model for estimating landslide-inducing rainfall, Journal of Geology, 102, https://doi.org/10.1086/629714, 1994.

Rengers, F. K., McGuire, L. A., Coe, J. A., Kean, J. W., Baum, R. L., Staley, D. M., and Godt, J. W.: The influence of vegetation on debris-flow initiation during extreme rainfall in the northern Colorado Front Range, Geology, 44, https://doi.org/10.1130/G38096.1, 2016.

Richards, L. A.: Capillary conduction of liquids through porous mediums, Journal of Applied Physics, 1, 318–333, https://doi.org/10.1063/1.1745010, 1931.

Richardson, P. W., Perron, J. T., and Schurr, N. D.: Influences of climate and life on hillslope sediment transport, Geology, 47, 423–426, https://doi.org/10.1130/G45305.1, 2019.

Rutz, J. J., Steenburgh, W. J., and Ralph, F. M.: Climatological Characteristics of Atmospheric Rivers and Their Inland Penetration over the Western United States, Monthly Weather Review, 142, 905–921, https://doi.org/10.1175/MWR-D-13-00168.1, 2014.

Saito, H. and Matsuyama, H.: Catastrophic Landslide Disasters Triggered by Record-Breaking Rainfall in Japan: Their Accurate Detection with Normalized Soil Water Index in the Kii Peninsula for the Year 2011, SOLA, 8, 81–84, https://doi.org/10.2151/SOLA.2012-021, 2012.

Saito, H., Nakayama, D., and Matsuyama, H.: Two Types of Rainfall Conditions Associated with Shallow Landslide Initiation in Japan as Revealed by Normalized Soil Water Index, SOLA, 6, 57–60, https://doi.org/10.2151/SOLA.2010-015, 2010.

Schmidt, K. M., Roering, J. J., Stock, J. D., Dietrich, W. E., Montgomery, D. R., and Schaub, T.: The variability of root cohesion as an influence on shallow landslide susceptibility in the Oregon Coast Range, Canadian Geotechnical Journal, 38, https://doi.org/10.1139/cgj-38-5-995, 2001.

Schuster, R. L. and Fleming, R. W.: Economic Losses and Fatalities Due to Landslides, Environmental & Engineering Geoscience, xxiii, 11–28, https://doi.org/10.2113/GSEEGEOSCI.XXIII.1.11, 1986.

https://doi.org/10.5194/egusphere-2024-873
Preprint. Discussion started: 3 April 2024

Seo, D. J. and Breidenbach, J. P.: Real-time correction of spatially nonuniform bias in radar rainfall data using rain gauge measurements, Journal of Hydrometeorology, 3, https://doi.org/10.1175/1525-7541(2002)003<0093:RTCOSN>2.0.CO;2, 2002.

Shields, C. A., Rutz, J. J., Leung, L.-Y., Ralph, F. M., Wehner, M., Kawzenuk, B., Lora, J. M., McClenny, E., Osborne, T., Payne, A. E., Ullrich, P., Gershunov, A., Goldenson, N., Guan, B., Qian, Y., Ramos, A. M., Sarangi, C., Sellars, S., Gorodetskaya, I., Kashinath, K., Kurlin, V., Mahoney, K., Muszynski, G., Pierce, R., Subramanian, A. C., Tome, R., Waliser, D., Walton, D., Wick, G., Wilson, A., Lavers, D., Prabhat, Collow, A., Krishnan, H., Magnusdottir, G., and Nguyen, P.: Atmospheric River Tracking Method Intercomparison Project (ARTMIP): project goals and experimental design, Geoscientific Model Development, 11, 2455–2474, https://doi.org/10.5194/gmd-11-2455-2018, 2018.

Smith, R. B., Schafer, P., Kirshbaum, D., and Regina, E.: Orographic Enhancement of Precipitation inside Hurricane Dean, Journal of Hydrometeorology, 10, 820–831, https://doi.org/10.1175/2008JHM1057.1, 2009.

Tao, S., Guo, Q., Li, C., Wang, Z., and Fang, J.: Global patterns and determinants of forest canopy height, Ecology, 97, 3265–3270, https://doi.org/10.1002/ECY.1580, 2016.

Thomas, M. A., Mirus, B. B., and Collins, B. D.: Identifying Physics-Based Thresholds for Rainfall-Induced Landsliding, Geophysical Research Letters, 45, 9651–9661, https://doi.org/10.1029/2018GL079662, 2018.

Thomas, M. A., Mirus, B. B., and Smith, J. B.: Hillslopes in humid-tropical climates aren't always wet: Implications for hydrologic response and landslide initiation in Puerto Rico, Hydrological Processes, 34, 4307–4318, https://doi.org/10.1002/HYP.13885, 2020.

Wills, C., Perez, F., and Branum, D.: New Method for Estimating Landslide Losses from Major Winter Storms in California and Application to the ARkStorm Scenario, Natural Hazards Review, 17, https://doi.org/10.1061/(asce)nh.1527-6996.0000142, 2016.

Wilson, R. C.: Rainstorms, pore pressures, and debris flows: a theoretical framework, in: Landslides in a Semi-Arid Environment, edited by: Sadler, P. M. and Morton, D. M., Publications of the Inland Geological Society, Riverside, CA, 101–117, 1989.

Wilson, R. C.: Normalizing rainfall/debris-flow thresholds along the U.S. Pacific coast for long-term variations in precipitation climate, in: Proceedings of the 1997 1st International Conference on Debris-Flow Hazards Mitigation: Mechanics, Prediction, and Assessment, San Francisco, CA, USA, 32–43, 1997.

Wilson, R. C. and Jayko, A. S.: Preliminary maps showing rainfall thresholds for debris-flow activity, San Francisco Bay region, California, Open-File Report, U.S. Dept. of the Interior, U.S. Geological Survey, https://doi.org/10.3133/ofr97745F, 1997.

Wilson, R. C. and Wieczorek, G. F.: Rainfall thresholds for the initiation of debris flows at La Honda, California, Environmental & Engineering Geoscience, 1, 11–27, 1995.

Wooten, R. M., Gillon, K. A., Witt, A. C., Latham, R. S., Douglas, T. J., Bauer, J. B., Fuemmeler, S. J., and Lee, L. G.: Geologic, geomorphic, and meteorological aspects of debris flows triggered by Hurricanes Frances and Ivan during

https://doi.org/10.5194/egusphere-2024-873
Preprint. Discussion started: 3 April 2024

September 2004 in the Southern Appalachian Mountains of Macon County, North Carolina (southeastern USA), Landslides,
875 5, 31–44, https://doi.org/10.1007/s10346-007-0109-9, 2008.